JCB Journal of Cell Biology

ARTICLE

A septin GTPase scaffold of dynein–dynactin motors triggers retrograde lysosome transport

Ilona A. Kesisova, Benjamin P. Robinson, and Elias T. Spiliotis

The metabolic and signaling functions of lysosomes depend on their intracellular positioning and trafficking, but the underlying mechanisms are little understood. Here, we have discovered a novel septin GTPase–based mechanism for retrograde lysosome transport. We found that septin 9 (SEPT9) associates with lysosomes, promoting the perinuclear localization of lysosomes in a Rab7-independent manner. SEPT9 targeting to mitochondria and peroxisomes is sufficient to recruit dynein and cause perinuclear clustering. We show that SEPT9 interacts with both dynein and dynactin through its GTPase domain and N-terminal extension, respectively. Strikingly, SEPT9 associates preferentially with the dynein intermediate chain (DIC) in its GDP-bound state, which favors dimerization and assembly into septin multimers. In response to oxidative cell stress induced by arsenite, SEPT9 localization to lysosomes is enhanced, promoting the perinuclear clustering of lysosomes. We posit that septins function as GDP-activated scaffolds for the cooperative assembly of dynein–dynactin, providing an alternative mechanism of retrograde lysosome transport at steady state and during cellular adaptation to stress.

Introduction

Lysosomes are major degradative organelles with critical functions in a diversity of cellular processes, including cell metabolism, signaling, gene regulation, and immunity (Blott and Griffiths, 2002; Lawrence and Zoncu, 2019; Settembre et al., 2013). Lysosomes contain membrane transporters of amino acids, nucleotides, lipids, and ions, which sense intracellular conditions and cross talk with signaling complexes that regulate autophagy and gene transcription (Li et al., 2019; Lim and Zoncu, 2016; Schwake et al., 2013). Lysosomes are dynamic organelles whose intracellular position and movement are critical for their signaling functions, maturation, turnover, and interaction with other membrane organelles (Bonifacino and Neefjes, 2017; Luzio et al., 2007; Saftig and Klumperman, 2009; Savini et al., 2019). In response to nutritional and oxidative stress, lysosomes mobilize to perinuclear areas of the cytoplasm, where they fuse with autophagosomes (Lim and Zoncu, 2016; Yim and Mizushima, 2020). Similarly, lysosomes traffic retrogradely to bacteria undergoing autophagy (Hu et al., 2020) and anterogradely to plasma membrane sites of repair (Andrews and Corrotte, 2018) and exocytose in migrating and immune cells (Castro-Castro et al., 2016; Lettau et al., 2007; Wilson et al., 2018).

How lysosomes mobilize in response to various intracellular conditions and cues is not well understood. Lysosome positioning and movement involve selective association with microtubule motors and subsets of microtubules with distinct posttranslational modifications (Bonifacino and Neefjes, 2017; Guardia et al., 2016; Mohan et al., 2019). Anterograde movement of lysosomes to the cellular periphery is mediated by motors of the kinesin-1, -2, and -3 families (Farías et al., 2017; Guardia et al., 2016; Matsushita et al., 2004; Pankiv et al., 2010; Rosa-Ferreira and Munro, 2011). Retrograde movement of lysosomes to the perinuclear cytoplasm is driven by the microtubule motor dynein. Association of dynein with lysosomes occurs through mechanisms that are linked to the metabolic sensing functions of lysosomes. Components of the dynein–dynactin complex interact directly with the calcium ion sensor ALG2 and the cholesterol-sensing Rab7–RILP–ORP1L complex (Li et al., 2016; Rocha et al., 2009). Additionally, dynein associates with the scaffold protein JIP4, which is recruited by the lysosomal transmembrane protein TMEM55B, whose levels are up-regulated in response to lysosomal stress (Willett et al., 2017). Despite this multimodal recruitment of dynein–dynactin, which indicates that lysosomes adopt a diversity of strategies for retrograde transport, it is little understood how dynein motility is activated on lysosomal membranes.

The discovery of adaptor proteins that promote the interaction of dynein with dynactin has revolutionized our understanding of dynein motility (Cross and Dodding, 2019; McKenney et al., 2014; Olenick and Holzbaur, 2019; Reck-Peterson et al., 2018). Dynein is a hexameric motor consisting of a dynein heavy

Department of Biology, Drexel University, Philadelphia, PA.

Correspondence to Elias T. Spiliotis: ets33@drexel.edu.

chain (DHC), an intermediate chain (DIC), a light intermediate chain (DLIC), and three light chains (Schmidt and Carter, 2016; Sweeney and Holzbaur, 2018). Dynactin is a large multisubunit complex that is made of a central actin-like filament, which is capped by proteins on its barbed (CAPZ) and pointed (ARP11, p62, p27, p25) ends, and a shoulder subcomplex containing $p150^{GLUED}$, p50 dynamitin, and p24 (Schroer, 2004). Dynein dimerizes into an autoinhibitory conformation, which is weakly processive and requires assembly with dynactin and activating adaptor proteins in order to move efficiently on microtubules (Chowdhury et al., 2015; McKenney et al., 2014; Schroer and Sheetz, 1991; Urnavicius et al., 2018; Zhang et al., 2017). Dynein adaptors contain coiled-coil domains that run along the central dynactin filament and promote dynein–dynactin binding by making contacts with both dynactin and the dynein heavy and light intermediate chains (Chowdhury et al., 2015; Lee et al., 2018; Olenick and Holzbaur, 2019; Schlager et al., 2014; Schroeder and Vale, 2016; Urnavicius et al., 2018). These coiled-coil domains, however, are not present in all dynein adaptors, including the lysosomal RILP and JIP4 (Reck-Peterson et al., 2018).

Septins are a family of GTP-binding proteins, which multimerize into higher-order oligomers and polymers that associate with cell membranes and the cytoskeleton (Mostowy and Cossart, 2012; Spiliotis, 2018). Membrane-bound septins function as scaffolds and diffusion barriers, which control protein localization in a spatiotemporal-specific manner (Bridges and Gladfelter, 2015; Caudron and Barral, 2009). In the endocytic pathway, septins associate preferentially with endolysosomes that are enriched with phosphatidylinositol 3,5-bisphosphate and Rab7 (Dolat and Spiliotis, 2016). Moreover, septins are critical for lysosome merging with macropinosomes and *Shigella* bacteria undergoing autophagy (Dolat and Spiliotis, 2016; Krokowski et al., 2018). In a proteomic study of the dynein interactome, septins were identified as potential binding partners of DIC, DLIC, and the dynein adaptor BiCD2 (Redwine et al., 2017). Here, we report that membrane-associated septins provide a novel GDP-activated mechanism for the retrograde dynein-driven transport of lysosomes.

Results

Septins associate with lysosomes and promote retrograde trafficking in a Rab7-independent manner

Septins have been reported to associate with membranes of the late endocytic pathway, localizing to mature macropinosomes and impacting the formation of multivesicular bodies (Dolat and Spiliotis, 2016; Traikov et al., 2014). However, it is unknown whether septins are functionally present on lysosomes. Using high- and super-resolution microscopy as well as subcellular fractionation, we probed for septin localization to lysosomes. We stained COS-7 cells with antibodies against septin 9 (SEPT9), a ubiquitously expressed septin and core subunit of heteromeric septin complexes (Kim et al., 2011; Sellin et al., 2011). As previously observed (Connolly et al., 2011; Verdier-Pinard et al., 2017), SEPT9 formed stress fiber–like filaments on the ventral side of the nucleus and localized to plasma membrane domains of curvature. Additionally, SEPT9 puncta were visible in perinuclear and peripheral regions of the cytoplasm. Confocal microscopy showed that a fraction of lysosomes and early endosomes, which were immunolabeled with antibodies against LAMTOR4 and EEA1, respectively, overlapped with SEPT9 filaments and puncta (Fig. 1, A and B). Quantitatively, SEPT9 puncta were present on lysosomes more abundantly than early endosomes (79.7% vs. 40.8%), indicating a preferential association with lysosomes (Fig. 1 C). SEPT9 puncta, however, covered 23% ± 0.4% of the total surface of lysosomes compared with 12% ± 0.4% of early endosomes per cell (n = 6), suggesting that SEPT9 localizes to subdomains of the lysosomal membrane. Super-resolution structured illumination microscopy showed that SEPT9 puncta localize to microdomains of the limiting membrane of LAMP2-positive compartments (Fig. 1 D). These SEPT9 microdomains resembled the clusters of LAMP2A and dynein motors, which have been previously observed on the membranes of late phagosomes and lysosomes (Kaushik et al., 2006; Rai et al., 2016). In living cells, SEPT9-mCherry (SEPT9 isoform 1), which was expressed under the weak phosphoglycerate kinase (PGK) promoter, also localized to microdomains of LAMP1-mGFP compartments (Fig. 1 E, arrows) and cotrafficked with LAMP1-mGFP compartments that moved retrogradely toward the nucleus (Fig. 1, F and G; and Video 1). In contrast, colocalization and cotraffic of SEPT9-mCherry with GFP-EEA1 was rare (Fig. S1, A and B). Consistent with septin localization to lysosomes, septins (SEPT2, SEPT6, SEPT7, and SEPT9) cofractionated with LAMP1- and Rab7-positive membranes at the top of an iodixanol (Optiprep) density gradient of human embryonic kidney cell (HEK293) extracts (Fig. S1 C). Notably, SEPT9 had the highest percentage (~14%) of total protein in the top LAMP1-enriched fraction than any other fraction, and other septins (e.g., SEPT6 and SEPT7) were also relatively more enriched in the top fraction (Fig. S1, C and D).

To test whether septins impact the intracellular position of lysosomes, we overexpressed SEPT9 in COS-7 cells. SEPT9-mCherry increased the perinuclear clustering of lysosomes, increasing the ratio of perinuclear to peripheral lysosomes (Fig. 1, H and I); high levels of nuclear and cytoplasmic SEPT9-mCherry concealed its lysosomal localization, which was observed in cells expressing SEPT9-mCherry under a weak promoter (Fig. 1, E and F). In contrast to the perinuclear clustering of lysosomes, the intracellular distribution of early endosomes did not change (Fig. S1, E and F), and overexpression of SEPT2 and SEPT6 did not impact lysosomal distribution (Fig. S1, G and H). Depletion of SEPT9 diminished the perinuclear population of lysosomes, exerting the opposite effect of SEPT9 overexpression (Fig. 1, J and K; and Fig. S1, I and J). This reduction was reversed with an shRNA-resistant SEPT9-GFP, which was expressed concomitantly with the shRNA against SEPT9, demonstrating that the phenotype was not due to an off-target effect (Fig. 1, J and K).

Given that retrograde dynein-driven transport of lysosomes is hitherto controlled by the small GTPase Rab7, we asked if Rab7 is required for the perinuclear clustering of lysosomes by SEPT9. Using a Rab7 dominant-negative (Rab7-DN) mutant, we quantified the intracellular distribution of lysosomes in COS-7 cells, which overexpressed SEPT9 in the presence or absence of

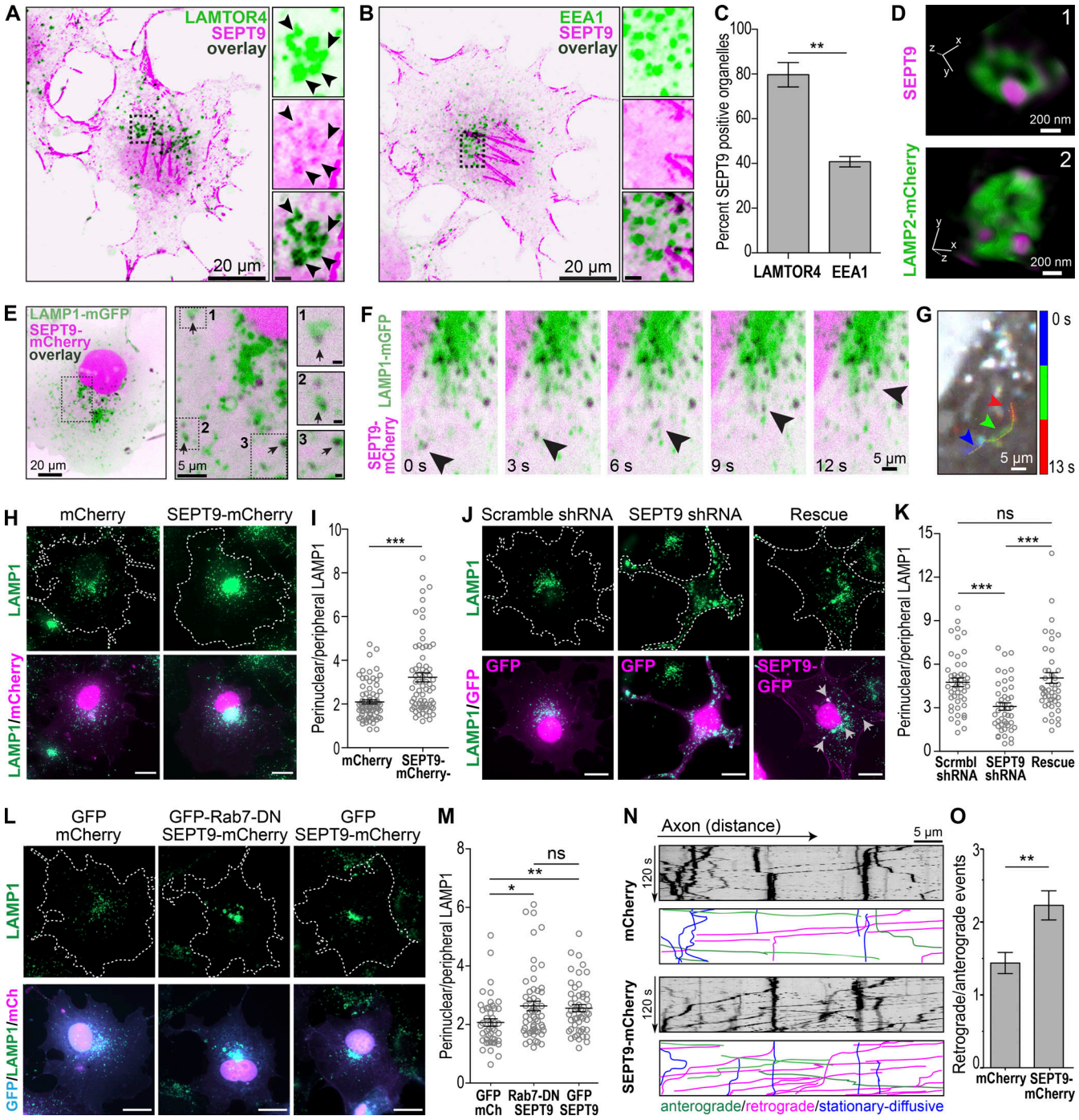

Figure 1. **Septins associate with lysosomes and promote lysosome positioning in the perinuclear cytoplasm. (A and B)** Confocal images of COS-7 cells stained for SEPT9 (inverted magenta) and LAMTOR4 (inverted green; A) or EEA1 (inverted green; B). Scale bars, 20 µm. Insets show lysosomes from perinuclear regions in higher magnification (scale bars, 3 µm). Arrowheads point to SEPT9 puncta that localize on LAMTOR4-stained lysosomes. **(C)** Bar graph shows percentage (mean ± SEM; Mann–Whitney *U* test) of LAMTOR4 and EEA1 organelles with SEPT9 puncta per cell (n = 6 cells). **(D)** Super-resolution structured illumination microscopy images show SEPT9 puncta on the delimiting membrane of LAMP2-mCherry–labeled compartments in BSC-1 cells. **(E and F)** Spinning-disk confocal microscopy image (E) and still frames from time-lapse imaging (F) of COS-7 cells transfected with SEPT9-mCherry and LAMP1-mGFP. Insets show higher-magnification LAMP1-mGFP compartments with SEPT9-mCherry puncta (arrows; scale bars, 1 µm), and arrowheads point to retrograde cotraffic toward the nucleus. Scale bar, 5 µm. **(G)** Color-coded trajectory of the SEPT9-positive lysosome moving retrogradely in F. Arrowheads point to the early (blue), medial (green), and late (red) stages of movement. **(H)** COS-7 cells were transfected with mCherry or SEPT9-mCherry and stained with anti-LAMP1. Scale bars, 20 µm. **(I)** Plot shows the ratio (mean ± SEM) of perinuclear to peripheral LAMP1 fluorescence intensity per cell (*n* = 70–79; Mann–Whitney *U* test). **(J)** Images of LAMP1-stained COS-7 cells after transfection with plasmids coexpressing scramble control or SEPT9-targeting shRNAs and GFP or SEPT9-GFP. Arrows point to lysosomes (LAMP1) with SEPT9-GFP. Scale bars, 20 µm. **(K)** Plot shows the ratio (mean ± SEM; Mann–Whitney *U* test) of perinuclear to peripheral LAMP1 fluorescence intensity per cell (*n* = 45–47). **(L)** Images show lysosome (LAMP-1) distribution in COS-7 cells transfected with mCherry and GFP, SEPT9-mCherry and GFP-Rab7-DN, or SEPT9-mCherry and GFP. Scale bars, 20 µm. **(M)** Quantification shows the ratio (mean ± SEM; Kruskal–Wallis one-

way ANOVA) of perinuclear to peripheral LAMP1 fluorescence intensity per cell (n = 45–51). **(N)** Embryonic (E18) hippocampal neurons (DIV4) were transfected with LAMP1-mGFP and mCherry or rat SEPT9-mCherry, and axons were imaged live by TIRF microscopy. Kymographs show stationary or diffusive (blue), retrogradely (magenta), or anterogradely (green) moving particles with LAMP1-mGFP. Scale bar, 5 µm. **(O)** Bar graph shows the ratio (mean ± SEM; unpaired t test) of retrogradely to anterogradely moving LAMP-1-mGFP particles/2 min per axon (n = 18–19). ns, nonsignificant (P > 0.05); *, P < 0.05; **, P < 0.01; ***, P < 0.001.

Rab7-DN. Rab7-DN did not alter the effects of SEPT9 overexpression, indicating that SEPT9 induces retrograde lysosome transport independently of Rab7 (Fig. 1, L and M).

Next, we sought to examine whether SEPT9 has a conserved role in lysosome positioning across different cell types. We tested if SEPT9 impacts lysosome traffic in primary rat embryonic hippocampal neurons. In early stages of neuronal morphogenesis, SEPT9 is present in the developing axon before it becomes enriched on dendritic microtubules (Karasmanis et al., 2018). In the axons of these cells, which consist of unidirectional plus-end-out–oriented microtubules, we found that SEPT9 was enriched more than twofold in LAMP1-positive endolysosomes compared with Rab5-containing early endosomes (Fig. S1, K and L). SEPT9 overexpression enhanced the retrograde trafficking events of axonal lysosomes, increasing the ratio of retrograde-to-anterograde events from 1.44 ± 0.15 to 2.23 ± 0.20 (Fig. 1, N and O; and Videos 2 and 3). Taken together with our observations in COS-7 cells, these data show that septins have a functional role in lysosome positioning and trafficking.

Membrane-associated SEPT9 induces retrograde trafficking by recruiting the dynein–dynactin complex

Because the perinuclear localization of lysosomes depends on SEPT9 expression, we hypothesized that SEPT9 induces retrograde lysosome transport by recruiting dynein–dynactin motors. To directly test this possibility, we generated SEPT9 chimeras that are coupled to the membrane of peroxisomes and mitochondria. Using the rapamycin-inducible FRB-FKBP dimerization system, we targeted GFP-SEPT9-FRB to peroxisomes containing PEX-RFP-FKBP. After 45 min of rapalog treatment, GFP-SEPT9-FRB colocalized with PEX-RFP-FKBP, and peroxisomes became clustered into a focal juxtanuclear region (Fig. 2 A). Quantification of the percentage of cells with a clustered peroxisome phenotype showed an increase from 35% to 81% after treatment with rapalog (Fig. 2 A). We observed similar perinuclear clustering of mitochondria upon expression of SEPT9-MitoTagRFP, a SEPT9 chimera that contains the mitochondrial-targeting signal of the *Listeria monocytogenes* protein ActA (Fig. 2 B). Perinuclear mitochondria were stained positively for the MitoSpy near-infrared (NIR) DiIC1 dye, which labels mitochondria with a healthy membrane potential, indicating that the perinuclear aggregation of mitochondria was not due to mitophagy (Fig. S2, A and B).

Next, we examined whether perinuclear clustering of mitochondria was due to microtubule-dependent dynein-driven transport. Depolymerization of microtubules with nocodazole and expression of the GFP-p50-dynamitin, which inhibits dynein-driven transport in a dominant-negative manner (Burkhardt et al., 1997), diminished the perinuclear aggregation of mitochondria, resulting in a more dispersed localization throughout the cytoplasm (Fig. 2, C and D). Notably, SEPT9-MitoTagRFP increased the mitochondrial levels of DIC, which remained above control levels upon microtubule depolymerization, indicating that SEPT9 recruits dynein to mitochondria independently of microtubule attachment (Fig. 2 E). Thus, mitochondria-targeted SEPT9 induces retrograde microtubule-dependent transport by promoting the recruitment of dynein.

To further test whether SEPT9 interacts with dynein, we performed coimmunoprecipitations and protein-binding assays. In HEK-293 cell lysates, SEPT9 coimmunoprecipitated with the dynein and dynactin subunits DIC and p150^{GLUED} (Fig. 2 F). Using native dynein and dynactin, which were isolated from HEK-293 cells, we tested whether recombinant SEPT9 interacted directly with dynein. SEPT9 pulled down DHC (dynein) and p150^{GLUED} (dynactin) while binding to SEPT2/6/7 was negligible (Fig. 2 G). Despite lack of SEPT2/6/7-dynein binding, targeting of SEPT2, SEPT6, or SEPT7 to mitochondria enhanced perinuclear clustering (Fig. S2, C and D), indicating that SEPT9 may function in complex with SEPT2/6/7, as mitochondria-targeted SEPT9 also recruited SEPT2, SEPT6, and SEPT7 to mitochondria (Fig. S2 E). SEPT9 depletion, however, impaired mitochondria clustering by MitoTagRFP-tagged SEPT2, SEPT6, or SEPT7, which shows that SEPT9 is a key subunit for retrograde transport (Fig. S2 F). Taken together, these data show that SEPT9 interacts directly and specifically with dynein–dynactin and, alone or in complex with SEPT2/6/7, triggers retrograde trafficking by recruiting the dynein motor.

SEPT9 interacts with both dynein and dynactin through its GTP-binding and N-terminal extension (NTE) domains, respectively

Activation of dynein-driven motility requires adaptor proteins that promote the assembly and stability of dynein–dynactin complexes. Activating dynein adaptors are characterized by long coiled-coil domains, which bridge dynein with dynactin by interacting concomitantly with subunits of the dynein–dynactin complex (Cross and Dodding, 2019; McKenney et al., 2014; Reck-Peterson et al., 2018). Thus, we sought to determine how SEPT9 interacts with dynein–dynactin.

SEPT9 consists of an NTE domain, which is largely disordered (Bai et al., 2016), and a GTP-binding domain (G domain) that is evolutionarily and structurally related to small GTPases. We purified recombinant versions of these domains and tested whether they interact directly with native dynein and dynactin. Strikingly, we found that the NTE and G domains have differential affinities for dynein and dynactin. The dynactin subunit p150^{Glued} was pulled down robustly with the NTE domain, but it was significantly less in pull-downs with the G domain of SEPT9 (Fig. 3 A). Conversely, the G domain associated strongly with DHC, which exhibited weaker binding to the NTE domain (Fig. 3 A).

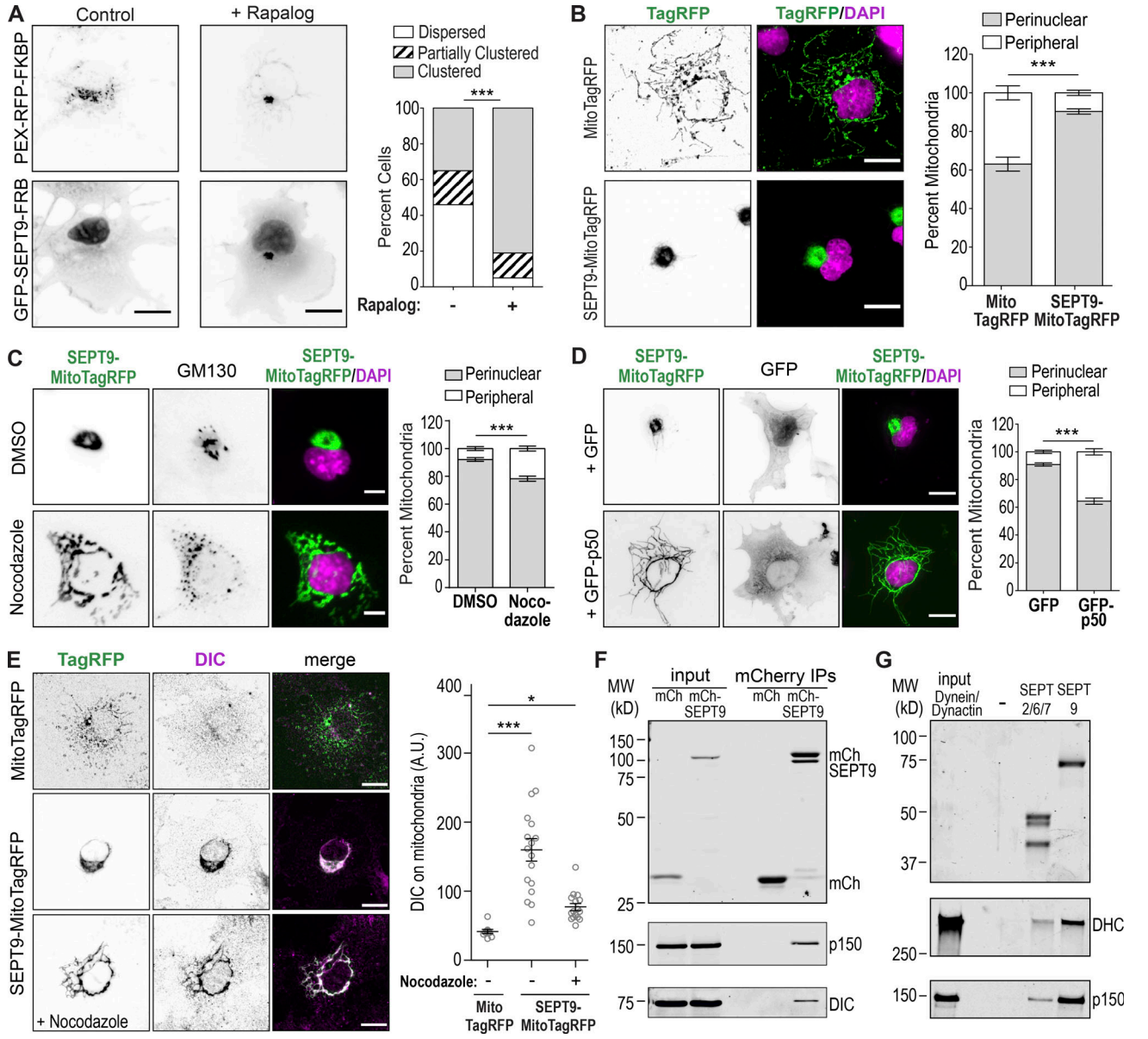

Figure 2. **Membrane-associated SEPT9 recruits dynein and induces retrograde dynein-driven transport. (A)** Images show COS-7 cells that were transfected with GFP-SEPT9-FRB and PEX-RFP-FKBP after 45 min of treatment with rapalog or control carrier. Bar graph shows percentage of cells (n = 37–42; χ^2 test) with dispersed, partially clustered, and clustered peroxisomes. Scale bar, 20 µm. **(B)** COS-7 cells were transfected with MitoTagRFP or SEPT9-MitoTagRFP and stained with DAPI. Bar graph shows perinuclear and peripheral mitochondria as percentage (mean ± SEM; two-way ANOVA) of total mitochondria per cell (n = 20–44). Scale bar, 20 µm. **(C)** COS-7 cells were transfected with Mito-TagRFP or SEPT9-MitoTagRFP, treated with nocodazole (33 µM) or DMSO for 3 h, and stained with anti-GM130 and DAPI. Quantification shows the amount of perinuclear and peripheral mitochondria as percentage (mean ± SEM; two-way ANOVA) of total mitochondria per cell (n = 53–54). Scale bar, 10 µm. **(D)** Images show DAPI-stained COS-7 cells that were transfected with SEPT9-MitoTagRFP and GFP (control) or GFP-p50 (dynamitin). Bar graph shows quantification of perinuclear and peripheral mitochondria as percentage (mean ± SEM; two-way ANOVA) of total per cell (n = 55–70). Scale bars, 20 µm. **(E)** COS-7 cells were transfected with MitoTagRFP or SEPT9-MitoTagRFP and stained with anti-DIC after 3-h treatment with DMSO or nocodazole (33 µM). Plot shows DIC fluorescence intensity (mean ± SEM) on MitoTagRFP-labeled mitochondria per cell (n = 9–16; Kruskal–Wallis one-way ANOVA). Scale bars, 20 µm. **(F)** Lysates of HEK-293 cells expressing mCherry or mCherry-SEPT9 were incubated with mRFP trap beads, and immunoprecipitates were blotted with antibodies against mCherry (top), DIC, and p150^{GLUED}. A.U., arbitrary units. **(G)** Coomassie-stained gel (top) shows recombinant SEPT9 and SEPT2/6/7, which were used in pull-down assays with dynein–dynactin purified from HEK-293 cells. Western blots (bottom) were performed with antibodies against DHC and p150^{GLUED}. *, P < 0.05; *** P < 0.001.

Hence, SEPT9 can interact with both dynein and dynactin through its GTP-binding and NTE domains, respectively.

To gain more insight into the SEPT9–dynein interactions, we examined if SEPT9 associates with domains of DLIC, which are critical for the activation of dynein motility by interacting directly with dynein adaptors. We tested if SEPT9 interacts with the C-terminus (aa 389–523) of DLIC, which is a common binding site for several dynein activators (Gama et al., 2017; Lee et al., 2018; Schroeder et al., 2014; Schroeder and Vale, 2016). SEPT9 did not bind DLIC(389–523) and similarly had a weak

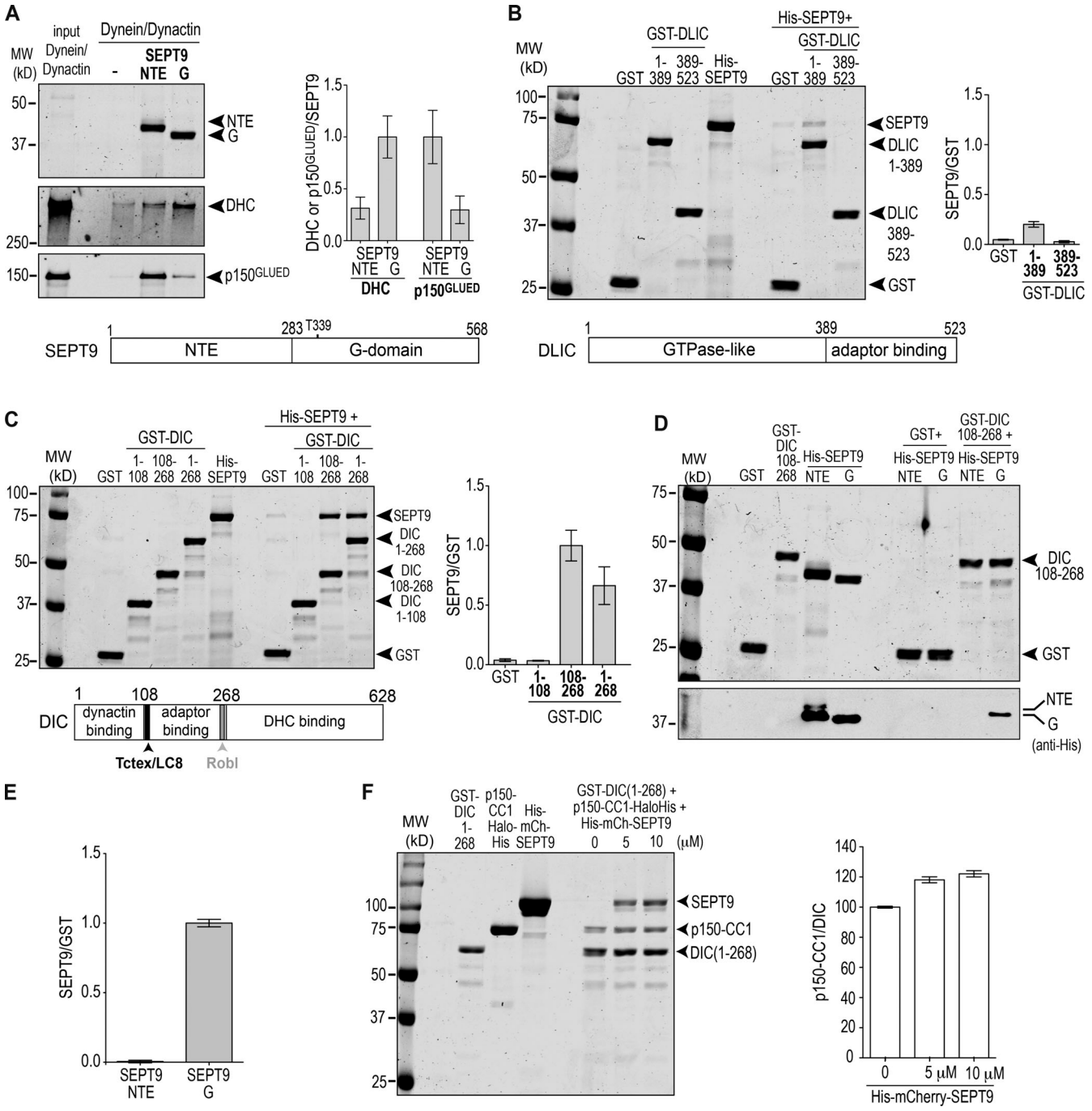

Figure 3. **SEPT9 provides a molecular link between dynein and dynactin through its GTP-binding and NTE domains, respectively. (A)** Coomassie-stained gel shows the recombinant NTE and G domains of SEPT9, which were used in pull-down assays with purified dynein and dynactin. Pull-downs were Western blotted with antibodies against DHC and p150^{GLUED}. Bar graph shows the mean ratio of DHC to NTE or G domain and p150GLUED to NTE or G domain fragments of His-SEPT9 intensities from three independent experiments; error bars indicate SEM. Schematic depicts the domains of SEPT9 and the position of the catalytic T339 residue required for GTPase activity. **(B)** Coomassie-stained gel shows the results of protein binding assays between recombinant His-SEPT9 and GST (control) or the GST-tagged N-terminal (aa 1–389) and C-terminal (aa 389–523) halves of DLIC. Bar graph shows the mean ratio of SEPT9 to GST or GST-DLIC protein band intensities from three independent experiments; error bars indicate SEM. Schematic depicts the GTPase-like and adaptor-binding domains of DLIC. **(C)** Coomassie-stained gel shows results from pull-down assays of His-SEPT9 with GST (control) or GST-tagged DIC(1–108), DIC(108–268), and DIC(1–268). Schematic shows the major domains of DIC and their corresponding interactions with components of the dynein–dynactin complex. Bar graph shows quantification of the relative amount of SEPT9 pulled down as the ratio (mean ± SEM) of SEPT9 to GST protein band intensities from five independent experiments. **(D)** Coomassie-stained gel (top) and Western blot (bottom; anti-His) show results from pull-down assays of recombinant NTE and G domain fragments of His-SEPT9 with GST-DIC(108–268). **(E)** Bar graph shows the mean ratio of NTE or G domain fragments of SEPT9 to GST-DIC(108–268) protein band intensities from three independent experiments; error bars indicate SEM. **(F)** Gel shows the input and results from protein binding assays of equimolar (0.5 μM) recombinant p150^{GLUED}-CC1-Halo-His with GST-DIC(1–268) in the presence of increasing concentrations of His-mCherry-SEPT9 (0, 5, and 10 μM). Bar graph shows the relative increase in the amount of DIC(1–268)-bound p150^{GLUED}-CC1 with increasing concentrations of SEPT9 from three independent experiments; ratio was set to 100 for 0 μM of SEPT9. Error bars indicate SEM.

affinity for the N-terminal domain of DLIC (Fig. 3 B). In contrast, SEPT9 interacted with the N-terminal domain of DIC (aa 1–268), which has been shown to associate with the snapin and huntingtin adaptors (Caviston et al., 2007; Di Giovanni and Sheng, 2015). While SEPT9 did not interact with the first 108 N-terminal amino acids of DIC, which associate with the p150^{GLUED} subunit of dynactin, it bound DIC(108–268), which interacts with dynein light chains and the dynein adaptor snapin (Fig. 3 C; Di Giovanni and Sheng, 2015). Full-length SEPT9 and its G domain interacted specifically with DIC(108–268), while neither the NTE domain of SEPT9 nor SEPT2/6/7 associated with DIC(108–268) (Fig. 3, D and E; and Fig. S3, A and B). These data indicate that SEPT9-dynein binding involves a direct interaction between the G domain of SEPT9 and DIC(108–268).

Given that the interaction of DIC with p150^{GLUED} is critical for the modulation of dynein motility (Ayloo et al., 2014; Culver-Hanlon et al., 2006; Feng et al., 2020; King and Schroer, 2000; Vaughan and Vallee, 1995), we tested whether SEPT9 impacts the association of the CC1 domain of p150^{GLUED} with the N-terminus of DIC. Using purified proteins, we assayed for direct binding of DIC(1–268) to p150^{GLUED}-CC1 in the presence of increasing concentrations of recombinant SEPT9. SEPT9 enhanced binding of p150^{GLUED}-CC1 to the N-terminal fragment of DIC by ∼20% (Fig. 3 F). Albeit modest, this was a reproducible effect with two different concentrations of SEPT9, suggesting that SEPT9 impacts DIC-p150^{GLUED} binding. Thus, similar to bona fide adaptors of dynein, SEPT9 interacts concomitantly with dynein and dynactin and may facilitate cooperative assembly into processive motor complexes.

SEPT9 functions as a GDP-activated switch of dynein-driven motility

Septins are a large family of paralogs, which vary in their ability to hydrolyze GTP (Sirajuddin et al., 2009; Zent et al., 2011; Zent and Wittinghofer, 2014). GTP-hydrolyzing septin paralogs such as SEPT9 assemble into functional oligomers and multimers that are bound to GDP (Castro-Castro et al., 2016). In contrast to monomeric small GTPases, which are active in their GTP-bound state, GTP-hydrolyzing septins are functionally active as GDP-bound multimers.

Association of SEPT9 with DIC through its G domain raised the possibility that SEPT9 interacts with dynein and induces dynein-driven transport in a nucleotide-dependent manner. To examine whether the G domain of SEPT9 interacts preferentially with DIC in its GTP- or GDP-bound state, we performed protein-binding assays with recombinant SEPT9 G domain and DIC(108–268) in the presence of GDP, GTP, and nonhydrolyzable guanosine 5′-*O*-[γ-thio]triphosphate (GTPγS). Strikingly, both GTP and nonhydrolyzable GTPγS abrogated SEPT9-DIC binding, which was observed only in the presence of GDP (Fig. 4 A). To further test whether SEPT9 binds DIC in its GDP-bound state, we mutated the catalytic threonine (T339) of the G domain into a glycine, a residue that is conserved in place of the catalytic threonine in septin paralogs that are constitutively bound to GTP (Sirajuddin et al., 2009). Compared with wild-type SEPT9 G domain, binding of the T339G mutant to DIC(108–268) was markedly reduced (Fig. 4 B). Thus, GTP hydrolysis is critical for the interaction of SEPT9 with dynein.

Next, we examined if the dynein-driven motility of membrane organelles is similarly sensitive to the nucleotide-bound state of SEPT9. Targeting of SEPT9(T339G) to mitochondria did not induce the perinuclear clustering observed with wild-type SEPT9 (Fig. 4, C and D). Moreover, SEPT9(T339G) failed to recruit DIC to mitochondria, demonstrating that membrane recruitment of DIC requires GDP-bound SEPT9 (Fig. 4, E and F). Overexpression of SEPT9(T339G) did not impact the intracellular position of lysosomes, which did not accumulate to the perinuclear cytoplasm as observed with SEPT9 (Fig. 4, G and H). Collectively, these data show that SEPT9 recruits dynein and induces dynein-driven motility in its GDP-bound state, which favors SEPT9 dimerization and assembly into higher-order multimers. Thus, SEPT9 provides a GDP-activated scaffold for the recruitment and assembly of dynein–dynactin motors.

SEPT9 promotes dynein-driven transport of lysosomes in response to acute oxidative stress

Our results suggest that SEPT9 provides a novel and alternative mechanism to the canonical small GTPase-based recruitment of dynein to lysosomes. In contrast to Rab7, which requires GTP, dynein recruitment by SEPT9 is GDP activated. We posited that this novel septin GTPase mechanism could be used in adaptive cellular responses to stress.

To investigate if SEPT9 is involved in the retrograde trafficking of lysosomes under conditions of cell stress, we induced acute oxidative stress with sodium arsenite ($NaAsO_2$), which triggers release of reactive oxygen species (Ellinsworth, 2015). After 30 min of arsenite treatment, there was a striking loss of subnuclear septin filaments and an amplification of perinuclear SEPT9 puncta (Fig. 5 A). Quantitatively, SEPT9 localization to lysosomes (LAMTOR4) was markedly enhanced in arsenite-treated cells (Fig. 5 B). Under conditions of glucose starvation, which primarily deprives cells of energy and secondarily induces the production of reactive oxygen species (Graham et al., 2012; Liu et al., 2003; Song and Hwang, 2018), SEPT9 filaments were not disrupted, and lysosomal levels of SEPT9 puncta did not increase (Fig. 5 B). Thus, enhancement of SEPT9 localization to lysosomes appears to occur specifically in response to arsenite-induced oxidative stress.

To determine whether SEPT9 contributes to the dynein-driven transport of lysosomes under oxidative stress, we analyzed the intracellular distribution of lysosomes in control and SEPT9-depleted cells after a 2-h treatment with sodium arsenite, which causes lysosomal congression to the perinuclear cytoplasm (Fig. 5, C and D; Willett et al., 2017). SEPT9 knockdown reduced the fraction of lysosomes in the perinuclear cytoplasm (Fig. 5, C and E). Expression of shRNA-resistant GFP-SEPT9 ameliorated the effects of the knockdown, increasing the fraction of lysosomes in between the cell center and periphery (Fig. 5, C and E). In contrast, the shRNA-resistant GFP-SEPT9(T339G) mutant, whose dynein-binding is impaired, did not improve the perinuclear clustering of lysosomes (Fig. 5, C and E). Notably, SEPT9(T339G) deteriorated the knockdown phenotype, causing clustering of lysosomes at regions of the cell periphery (Fig. 5 C, arrows). This phenotype is reminiscent of the peripheral accumulation of lysosomes in cells depleted of the dynein adaptor

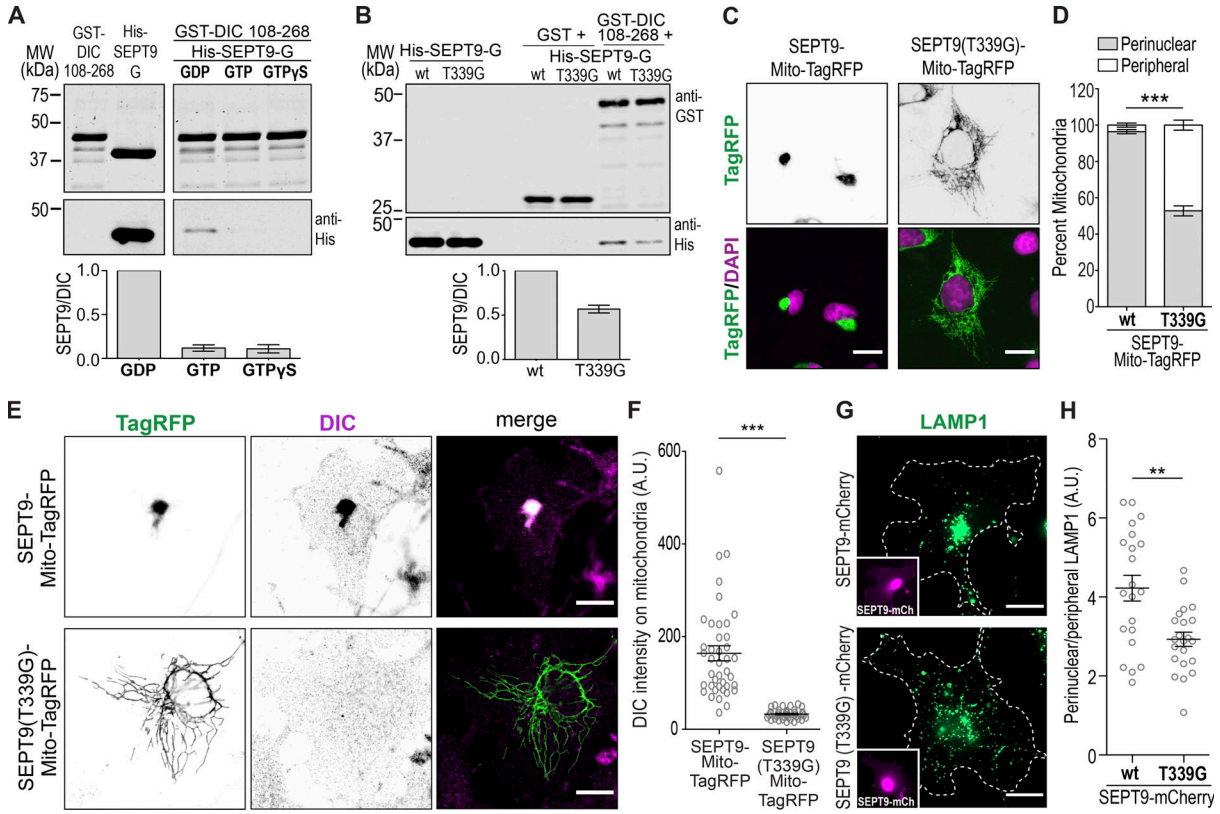

Figure 4. **The GDP-bound state of SEPT9 recruits dynein and induces retrograde transport. (A)** Coomassie-stained gel (top) and Western blot (bottom; anti-His) show binding of the G domain of SEPT9 to GST-DIC(108–268) in the presence of GDP, GTP, or GTPγS (0.5 mM). Quantification shows the relative ratios of SEPT9 G domain to GST-DIC(108–268) protein band intensities from three independent experiments. **(B)** Gels show Western blots (anti-GST/anti-His) of pull-downs of recombinant His-tagged wild-type (wt) or GTPase-dead (T339G) SEPT9 with GST or GST-DIC(108–268). Bar graph shows the relative ratio of the wild-type or GTPase-dead (T339G) G domain of SEPT9 to GST-DIC(108–268) from four independent experiments. Error bars indicate SEM. **(C)** Images show DAPI-stained COS-7 cells transfected with mitochondria-targeted (Mito-TagRFP) wild-type and GTPase-dead (T339G) SEPT9. Scale bars, 20 µm. **(D)** Bar graph shows perinuclear and peripheral mitochondria as percentage (mean ± SEM; two-way ANOVA) of total mitochondria per cell (n = 24–27). Error bars indicate SEM. **(E)** Images show COS-7 cells transfected with mitochondria-targeted (MitoTagRFP) wild-type or GTPase-dead (T339G) SEPT9 and stained with an antibody against DIC. Scale bars, 20 µm. **(F)** Plot shows DIC fluorescence intensity (mean ± SEM; Mann–Whitney U test) on mitochondria with SEPT9-Mito-TagRFP or SEPT9(T339G)-Mito-TagRFP per cell (n = 40–41). **(G)** Images show the distribution of lysosomes (LAMP-1) in COS-7 cells transfected with wild-type SEPT9-mCherry or SEPT9(T339G)-mCherry (insets). Scale bars, 20 µm. **(H)** Plot shows the ratio (mean ± SEM; unpaired t test) of perinuclear to peripheral LAMP1 fluorescence intensity per cell (n = 21–22). **, P < 0.01; ***, P < 0.001. A.U., arbitrary units.

JIP4 (Willett et al., 2017). To rule out the possibility that these effects were cell type specific, we induced oxidative stress with sodium arsenite in HeLa cells and examined how SEPT9 knockdown and rescue with wild-type or mutant SEPT9 impacts the perinuclear positioning of lysosomes. SEPT9 knockdown abrogated lysosome clustering, which was diminished to untreated levels (Fig. 5, F and G; and Fig. S4, A–C). Perinuclear accumulation was restored by shRNA-resistant GFP-SEPT9 but not GFP-SEPT9-T339G, which enhanced lysosome localization to the cell periphery (Fig. 5, F and G; and Fig. S4 C, arrows). Taken together, these data demonstrate that SEPT9 is critical for the retrograde transport of lysosomes under conditions of oxidative stress.

Discussion

The intracellular traffic and position of lysosomes are critical for their biogenesis, turnover, and physiological functions. In response to a variety of metabolic and signaling cues, lysosomes mobilize by recruiting kinesin and/or dynein motors, but the underlying mechanisms are not well understood. Here, we have discovered a novel mechanism of dynein-driven motility, which is mediated by SEPT9, a GTPase of the septin family. Unlike the Rab7 GTPase and lysosomal membrane proteins, which recruit dynein through cytoplasmic adaptor proteins (e.g., RIPL, JIP4, and ALG4), SEPT9 is a membrane-associated GTPase that interacts directly with dynein. Notably, SEPT9 associates preferentially with dynein in its GDP-bound state, which favors SEPT9 dimerization and assembly into higher-order oligomers. Hence, in contrast to the monomeric small GTPases of the Rab and Arf families, which are activated by GTP, SEPT9 provides a GDP-activated scaffold for the recruitment of multiple dynein–dynactin complexes. This scaffolding function may facilitate cooperative assembly of dynein–dynactin into the nanodomains of motor teams, which have been observed on lipid microdomains and microtubules (Cella Zanacchi et al., 2019; Rai et al., 2016).

Our results indicate that SEPT9 provides a mechanism for lysosome transport under conditions of oxidative stress. It is

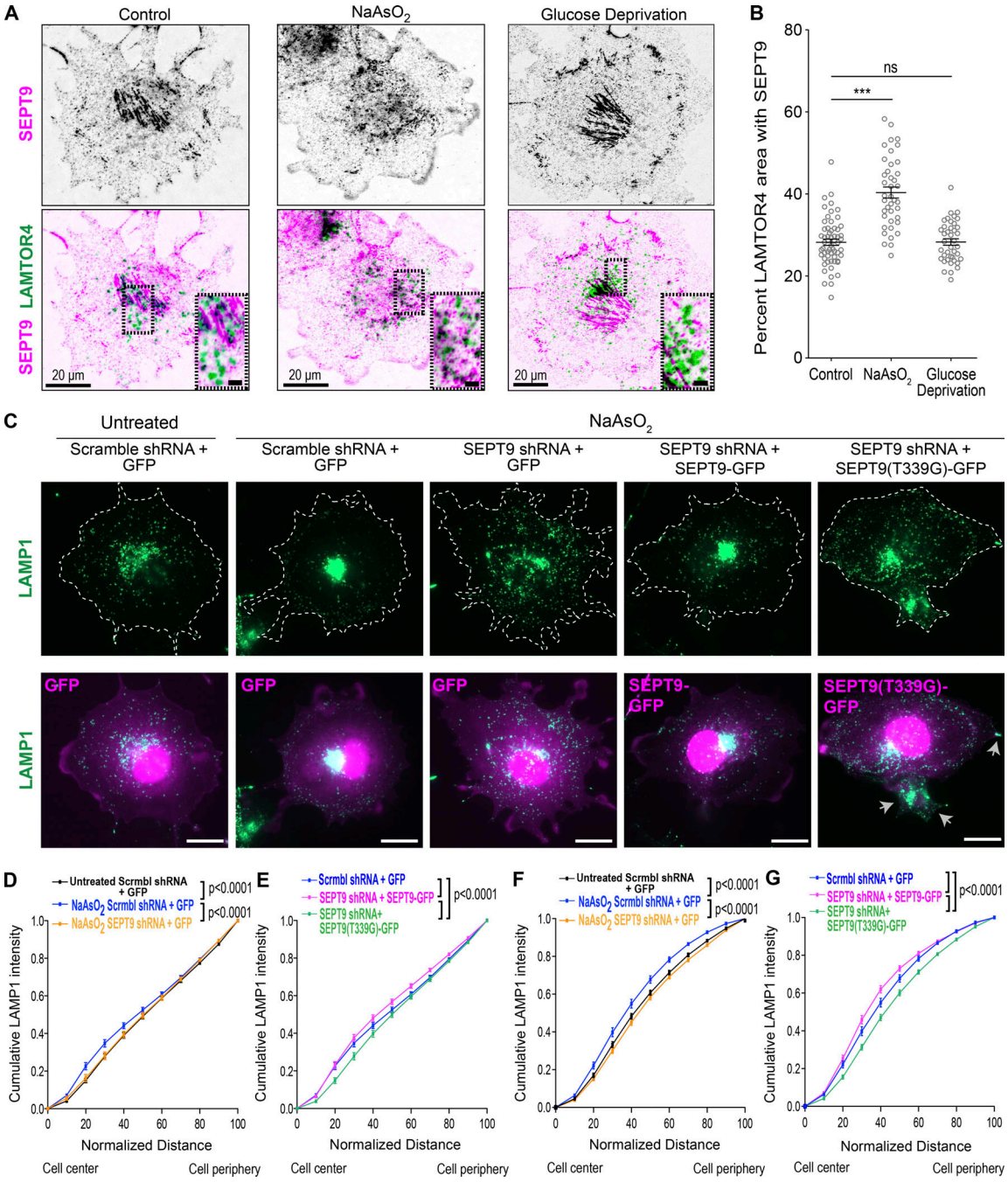

Figure 5. **Oxidative stress increases lysosomal levels of SEPT9, which promotes perinuclear clustering. (A)** Confocal microscopy images (inverted monochrome) of COS-7 cells treated with $NaAsO_2$ (300 µM) for 30 min or deprived of glucose for 1 h and stained for LAMTOR4 (inverted green) and SEPT9 (inverted magenta). Scale bars, 20 µm. Insets show the outlined perinuclear regions in higher magnification. Scale bars, 5 µm. **(B)** Bar graph shows the percentage (mean ± SEM; unpaired *t* test) of total lysosomal area (LAMTOR4) that overlaps with endogenous SEPT9 per cell (n = 40–59) after $NaAsO_2$ treatment (300 µM, 30 min) or glucose deprivation (1 h). **(C)** COS-7 cells were transfected with plasmids that coexpress scramble control or SEPT9 shRNAs and GFP or shRNA-resistant SEPT9-GFP (wild type or T339G mutant). Images show lysosome (LAMP1) localization (green) and GFP fluorescence (magenta) after treatment with $NaAsO_2$ (300 µM) for 2 h. Arrows point to peripheral clusters of lysosomes. Scale bars, 20 µm. **(D and E)** Plots show the fraction (mean ± SEM; extra sum of squares *F* test) of total LAMP1 intensity across the distance of the cell radius, from the cell center to the periphery, after normalization for the length of each cell (n = 31–37). **(F and G)** HeLa cells were transfected with plasmids that coexpress scramble control or SEPT9 shRNAs and GFP or shRNA-resistant SEPT9-GFP (wild type or T339G mutant). Cells were stained with anti-LAMP1 after treatment with $NaAsO_2$ (400 µM) for 1 h. Plots show the fraction (mean ± SEM; extra sum of squares *F* test) of total LAMP1 intensity across the distance of the cell radius after normalization for the length of each cell (n = 55–64). ns, nonsignificant (P > 0.05); ***, P < 0.001.

unclear whether SEPT9 interfaces with the signaling pathways that trigger transcriptional up-regulation and posttranslational modifications of lysosomal proteins (e.g., TMEM55B) that recruit dynein adaptors. The oligomerizing properties of septins suggest that they may provide a faster means of dynein recruitment than mechanisms that require signal transduction to the nucleus. Interestingly, however, SEPT9 interacts with JNK, which also associates with the dynein adaptor JIP4 that is recruited by TMEM55B (Gonzalez et al., 2009). Thus, SEPT9 may be downstream of signaling pathways that trigger dynein recruitment to lysosomes through alternative mechanisms. Future work will explore if SEPT9 is linked to signaling pathways and lysosomal proteins with established roles in the retrograde transport of lysosomes in response to cell stress.

Among the members of the septin family of GTPases, SEPT9 is unique in possessing a faster GTPase activity and a dimerization interface, which is characterized by nucleotide-dependent plasticity (Castro et al., 2020; Zent and Wittinghofer, 2014). Additionally, SEPT9 has been reported to function and localize independently of its heteromeric partners as the central subunit of the octameric SEPT2/6/7/9 complex (Estey et al., 2010; Karasmanis et al., 2018). Our results indicate that SEPT9 interacts with dynein independently of SEPT2/6/7 but do not rule out the possibility that SEPT9 functions in a complex with SEPT2/6/7 on lysosomal membranes; a new study showed that SEPT7 coimmunoprecipitates with p150^{GLUED} (Chen et al., 2020). The faster hydrolytic activity of SEPT9 may select for its homomeric assembly and concomitantly favor dynein binding. Recent crystallographic studies show that GDP shifts the dimeric interface between the N- and C-termini of SEPT9 into a distinct open conformation, which has not been observed in other septin paralogs (Castro et al., 2020). This shift from a closed GTP-bound to an open GDP-bound interface impacts differentially the two polybasic membrane-binding domains of SEPT9, one of which becomes occluded while the other disengages from a neutralizing polyacidic domain (Castro et al., 2020; Omrane et al., 2019). Therefore, the GDP-bound SEPT9 could interact with dynein while in a membrane-binding mode that favors association with lysosomes.

Similar to dimeric bona fide dynein adaptors, which activate the processive motility of dynein, SEPT9 interacts concomitantly with dynein and dynactin. However, SEPT9 lacks the DLIC-binding domains and coiled-coil sequences of activating adaptors, and we were not able to observe an enhancement of dynein processivity in single-molecule in vitro motility assays. If SEPT9 alone is not sufficient to activate dynein–dynactin motility, we surmise that it provides a scaffold for the assembly of multiple dynein complexes, whose activation depends on the recruitment of additional factors (Rai et al., 2016; Urnavicius et al., 2018). Additionally, SEPT9 may reinforce dynein tethering to the membrane cargo and/or microtubules, facilitating movement under high load. As a dynein scaffold, SEPT9 could also coordinate dynein movement with kinesin motors. Notably, SEPT9 interacts with the cargo-binding C-terminal tail of kinesin-2/KIF17 (Bai et al., 2016) and therefore may provide a mechanism for switching between microtubule motors of opposite directionality as previously shown for JIP1, which triggers a dynein-kinesin switch upon phosphorylation by JNK (Fu and Holzbaur, 2013).

Previous studies have implicated septins in endocytic trafficking to lysosomes and autophagic-lysosomal delivery, both of which involve dynein-mediated transport (Song et al., 2016). Septins are critical for the biogenesis of multivesicular bodies (Traikov et al., 2014), and SEPT9 associates with TSG101, a component of the endosomal sorting complex required for transport (ESCRT) that binds ubiquitinated cargo and receptors (Karasmanis et al., 2019). It is plausible that SEPT9 links TSG101 to dynein, selecting for the retrograde flux of endosomes and multivesicular bodies with ubiquitinated proteins toward lysosomes. The dynein adaptor RILP has been similarly observed to interact with the ESCRT-II subunits Vps22 and Vps36 and is required for the biogenesis of multivesicular endosomes and the degradation of epidermal growth factor receptors (Progida et al., 2007; Progida et al., 2006). A septin-mediated retrograde transport of lysosomes and autophagosomes may also promote the autophagic destruction of pathogenic bacteria such as *Shigella flexneri*, which are entrapped in septin cage-like structures (Torraca and Mostowy, 2016). Septins are required for the recruitment of autophagic components to encaged bacteria and subsequent merging with lysosomes (Krokowski et al., 2018; Mostowy et al., 2010), which might be facilitated by retrograde movement to the cell center.

Considering that SEPT9 associates with microtubules, our findings pose the question of whether and how SEPT9 functions in dynein-driven traffic as both a microtubule-associated protein and membrane scaffold/adaptor. Results from in vitro motility assays have indicated that microtubule-associated SEPT9 inhibits dynein motility (Karasmanis et al., 2018), while membrane-associated SEPT9 promotes dynein-mediated transport. While these roles are not mutually exclusive, SEPT9 could shift from microtubules to endomembranes in response to cellular conditions and signaling cues. In serum-starved cells, loss of filamentous cytoskeleton-associated septins has been reported previously (Kinoshita et al., 1997), and our data show that SEPT9 localization to lysosomes is enhanced under cell stress. The N-terminal domain of SEPT9, which interacts with microtubules and actin filaments, contains a number of putative phosphorylation sites, indicating that SEPT9 localization is under phosphoregulation by signaling kinases. Hence, an on-demand shift of SEPT9 from microtubules to lysosomes would enable dynein-driven movement without interference from microtubule-associated SEPT9 molecules. Interestingly, this shift might be a property that characterizes a number of microtubule-associated proteins, including the dynein adaptor HOOK-1, that associate with both microtubules and membrane organelles (Krtková et al., 2016; Lindén et al., 1989; Maldonado-Báez et al., 2013; Tortosa et al., 2017).

In sum, our findings bear broader significance for dynein-driven transport and cellular adaptation to stress. Beyond lysosomes, septins can function as membrane scaffolds for the assembly and activation of dynein–dynactin complexes on a variety of endomembrane organelles and plasma membrane domains of micron-scale curvature, which favors membrane-septin binding. For example, septins could recruit dynein–dynactin

on organelles such as lipid droplets, whose growth and perinuclear accumulation depends on SEPT9 during hepatitis C virus infection (Akil et al., 2016). Alternatively, septins can facilitate dynein-mediated capture and tethering of microtubules at cortical membrane sites and possibly enable dynein-mediated microtubule focusing and sliding (Hendricks et al., 2012; Ligon et al., 2001; Tanenbaum et al., 2013). Importantly, under conditions of GTP shortage or low GTP/GDP ratios, septins could provide a mechanism of dynein–dynactin motility, which can be activated by GDP rather than GTP as needed for the small GTPases such as Rab7. Recent findings of activation of mTORC2 by Rho-GDP suggest that GTPase modules can adopt GDP-activated functions (Senoo et al., 2019). Notably, a reduction in GTP/GDP ratio has been shown to alter the oligomeric partners of yeast septins, which assemble into higher-order complexes with unique curvature and membrane-recognition properties (Garcia et al., 2011; Taveneau et al., 2020; Weems and McMurray, 2017). Thus, a GDP-triggered assembly of septins into scaffolding complexes that associate with lysosomal membranes might provide an adaptive GDP-sensing mechanism for the dynein-driven transport of lysosomes under conditions of cell stress.

Materials and methods

Antibodies and reagents

Cells were immunostained with the following antibodies: mouse anti-Lamp1 (1:100; H4A3 clone; Iowa Developmental Studies Hybridoma Bank), rabbit anti-SEPT9 (1:100; 10769-1-AP; Proteintech Group), rabbit anti-SEPT9 (1:200; NBP2-13294; Novus Biologicals), mouse anti-SEPT9 clone 10C10 (1:100; MABE992; Millipore-Sigma), rabbit anti-SEPT2 (N5N; 1:300; gift from Makoto Kinoshita, Nagoya University, Nagoya, Japan), rabbit anti-SEPT7 (1:300; 18991; IBL America), rabbit anti-SEPT6 (1:300; gift from Makoto Kinoshita), mouse anti-GM130 (1:200; 610823; BD Biosciences), mouse anti-DIC antibody clone 74.1 (1:100; MAB1618; Millipore), rabbit anti-LAMTOR4 (1:200; 12284S; Cell Signaling), and mouse anti-EEA1 clone 14/EEA1 (1:100; 610456; BD Biosciences). $F(ab')_2$ fragment affinity-purified secondary antibodies (1:200) were purchased from Jackson ImmunoResearch Laboratories and included donkey anti-mouse, anti-rabbit, and anti-chicken antibodies conjugated with aminomethylcoumarin acetate (mouse, 715-156-151), Alexa Fluor 488 (mouse, 715-546-150; rabbit, 711-546-152), Alexa Fluor 594 (mouse, 715-586-150; rabbit, 711-586-152), or Alexa Fluor 647 (mouse, 715-606-151; rabbit, 711-606-152). Cells were counterstained with DAPI (D9542; Sigma-Aldrich), Phalloidin CF405 (1:200; 00034-T; Biotium), or MitoSpy NIR DiIC1 dye (50 nm; 424807; BioLegend) as indicated and according to the manufacturer's instructions. Western blots were performed with mouse anti-Lamp1 (1:500; H4A3 clone; Iowa DSHB), rabbit anti-SEPT9 (1:1,000; 10769-1-AP; Proteintech Group), rabbit anti-SEPT2 (5N5 1:2,000; gift from Makoto Kinoshita), rabbit anti-SEPT7 (1:2,000; 18991; IBL America), rabbit anti-SEPT6 (1:1,000; gift from Makoto Kinoshita), mouse anti-GM130 (1:1,000; 610823; BD Biosciences), mouse anti-Rab7A (1:500; ab50533; Abcam), rabbit anti-Rab5 (1:500; sc-46692; Santa Cruz), mouse anti-BiP/GRP78 (1:500; 610978; BD Biosciences), mouse anti-DIC antibody clone 74.1 (1:1,000; MAB1618; Millipore), mouse anti-$p150^{Glued}$ (1:1,000; 610473; BD Biosciences), rabbit anti-mCherry (1:2,000; ab167453; Abcam), rabbit anti-DynC1H1 (1:500; 12345-1-AP; Proteintech Group), mouse anti-His tag (1:2,000; 34660; Qiagen), and rabbit anti-GST (1:2,000; sc 459; Santa Cruz). Secondary antibodies for Western blots (1:10,000) were purchased from LI-COR, including donkey anti-mouse 800CW (926-6873) and anti-rabbit 680RD (926-32212) conjugates. Nucleotides were purchased from Sigma-Aldrich (GTPγS and GDP) and Cytoskeleton (GTP). RFP trap agarose beads were purchased from ChromoTek.

Plasmids and constructs

Plasmids encoding for GFP-EEA1 were a gift from Silvia Corvera (University of Massachusetts Medical School, Worcester, MA; Addgene plasmid 42307; RRID:Addgene_42307; Lawe et al., 2000), LAMP1-mGFP was a gift from Esteban Dell'Angelica (University of California, Los Angeles, Los Angeles, CA; Addgene plasmid 34831; RRID:Addgene_34831; Falcón-Pérez et al., 2005), pGEX6P1-human LIC1 G domain (GST-LIC 1–389) was a gift from Ron Vale (University of California, San Francisco, San Francisco, CA; Addgene plasmid 74598; RRID:Addgene_74598; Schroeder et al., 2014), pGEX6P1-human LIC1 C-terminal half (GST-LIC 389–523) was a gift from Ron Vale (Addgene plasmid 74599; RRID:Addgene_74599; Schroeder et al., 2014), and EGFP-Rab7A T22N was a gift from Qing Zhong (University of California, Berkeley, Berkeley, CA; Addgene plasmid 28048; RRID:Addgene_28048; Sun et al., 2010). The plasmid for PEX-RFP-FKBP (Kapitein et al., 2010) was a gift from Casper Hoogenraad (Utrecht University, Utrecht, Netherlands), GFP-p50 dynamitin (Quintyne et al., 1999) was a gift from Trina Schroer (John Hopkins University, Baltimore, MD), and MitoTagRFP (N1-TagRFP-ActA; Sirianni et al., 2016) was donated by Adam Kwiatkowski (University of Pittsburgh, Pittsburgh, PA). Plasmids expressing recombinant GST-DIC(108–268) and GST-DIC(1–268) were kindly donated by Dr. Zu-Hang Sheng (National Institutes of Health, Bethesda, MD; Di Giovanni and Sheng, 2015), $p150^{GLUED}$-CC1-Halo-6xHis (aa 216-547) was a kind gift from Dr. Erika Holzbaur (University of Pennsylvania, Philadelphia, PA; Ayloo et al., 2014), and sfGFP-BICD2 (aa 25-400) was provided by Dr. Richard McKenney (University of California, Davis, Davis, CA; McKenney et al., 2014).

The plasmids GFP-Rab5A (Dolat and Spiliotis, 2016), mCherry-N1-humanSEPT9_i1 (Bai et al., 2013), mCherry-C1-humanSEPT9_i1 (Dolat et al., 2014), mCherry-N1-SEPT2 (Bowen et al., 2011), pmCherry-N1-ratSEPT9, and pET28a-mCherry-humanSEPT9 (Karasmanis et al., 2018), pET28a-SEPT9(i1), pET28a-SEPT9-NTE (aa 1–283), and pET28a-SEPT9G (aa 283–586; Bai et al., 2016) were constructed as previously described. The pnEA-vH and pnCS vectors encoding for His-SEPT2 and SEPT6/7-strep, respectively, have been described previously (Nakos et al., 2019).

Plasmids encoding for mitochondria-targeted septins were made as follows: mouse SEPT2, human SEPT6, and rat SEPT7 were PCR amplified using the primers 5′-CATCTCGAGATGTCT AAGCAACAAC-3′ and 5′-ACTGGATCCCACACATGCTGCCCGAG-3′, 5′-CATCTCGAGATGGCAGCGACCGATATAG-3′ and 5′-ACT

GGATCCCAATTTTTCTTCTCTTTGTC-3′, and 5′-CATCTCGAG ATGTCGGTCAGTGCG-3′ and 5′-ACTGGATCCCAAAAGATCTTG CCTTTC-3′, respectively, and inserted in the pTagRFP-Mito plasmid using XhoI and BamHI sites. Human SEPT9_i1 (NM_001113491.2) was PCR amplified using the primers 5′-CATCTC GAGATGAAGAAGTCTTAC-3′ and 5′-ACTAAGCTTCATCTCTGG GGCTTC-3′ and inserted into pTagRFP-Mito using XhoI and HindII sites. pmCherry-C1-SEPT6 was constructed by PCR amplification of human SEPT6 using the primers 5′-TCGAAGCTT CCATGGCAGCGACCGATATAG-3′ and 5′-TCGGGATCCTTAATT TTTCTTCTC-3′ and subsequently cloned into pmCherry-C1 with HindIII/BamHI sites. To construct pmCherry-SEPT9-PK, SEPT9-mCherry (NM_001113491.2) was subcloned from pmCherry-N1-SEPT9 into the NheI and NotI sites of the pcDNA-PGK-MCS-Hyg (gift from Dr. Kay Oliver Schink, Norwegian Radium Hospital, Oslo, Norway).

pEGFP-C2-SEPT9-FRB was constructed by inserting FRB sequence, amplified from GFP-BICDN-FRB (gift from Casper Hoogenraad; Hoogenraad et al., 2003), into pEGFP-C2 vector using EcoRI and BamHI. SEPT9 (NM_001113491.2) was subsequently cloned into the pEGFP-C2-FRB plasmid with XhoI/HindIII using the following primers: 5′-AAAAAACTCGAGCAT GAAGAAGTCTTACTCA-3′ and 5′-TTTTTTAAGCTTGACATCTCT GGGGCTT-3′. pGEX-KT-ext-DIC aa 1–108 (mouse IC1A) was created by inserting the PCR-amplified fragment of DIC using the primers 5′-AAAAAAGGATCCATGTCTGACAAGAGCGAC-3′ and 5′-TTTTTTCTCGAGCTACTGCAGGGTCCT-3′ with BamH1/XhoI. For constructing targeting SEPT9 shRNA (5′-GCACGATAT TGAGGAGAAA-3′) against human and monkey SEPT9 and scrambled nontargeting shRNA control (5′-GCGAAGAAGGAT ACGTAAT-3′), targeting sequences were inserted into the pSuper-GFP vector. Targeting sequence of SEPT9 shRNA was designed using BLOCK-iT RNAi Designer (Thermo Fisher Scientific), and the sequence was scrambled using the InvivoGen shRNA wizard. For constructing a rescue construct coexpressing SEPT9 shRNA with shRNA-resistant SEPT9, SEPT9 i1-GFP was PCR amplified from pEGFP-N1-SEPT9_i1 (Bai et al., 2016) using the primers 5′- AAAAAAACCGGTATGAAGAAGTCT TACTCAG-3′ and 5′-TTTTTTTGTACAGCTCGTCCATGCC-3′ and subsequently inserted into pSuper-GFP–expressing SEPT9 shRNA with AgeI and BsrGI. GFP sequence was removed from pSuper-GFP SEPT9 shRNA vector using the same enzymes. The AgeI restriction site in pEGFPN1 was mutagenized before SEPT9_i1-GFP subcloning into the pSuper-GFP SEPT9 shRNA vector using the following primers: 5′-CCCGGGATCCACCAGTAGCCACCATGGTGA-3′ and 5′-TCACCATGGTGGCTACTGGTGGATCCCGGG-3′. Next, SEPT9 i1 sequence was mutagenized at six different sites, creating silent mutations that introduce mismatches with the SEPT9 shRNA target sequence and confer shRNA resistance. These mutations were introduced sequentially using the following sets of primers: 5′- GATCAAGTCCATCACGCATGACAT AGAGGAGAAAGGCGTCCGG-3′ and 5′-CCGGACGCCTTTCTC CTCTATGTCATGCGTGATGGACTTGATC-3′; and subsequently 5′-TCAAGTCCATCACGCATGACATAGAAGAAAAGGGCGTCC GGATGA-3′ and 5′-TCATCCGGACGCCCTTTTCTTCTATGTCAT GCGTGATGGACTTGA-3′. The rescue construct coexpressing SEPT9 shRNA with shRNA-resistant SEPT9-GFP harboring the T339G mutation was constructed by point-directed mutagenesis using the following primers: 5′-GGAGCGCATCCCCAAGGGCAT CGAGATCAAGTCC-3′ and 5′-GGACTTGATCTCGATGCCCTTGGG GATGCGCTCC-3′. pET-28a-SEPT9-G domain-T339G, pTagRFP-Mito-SEPT9-T339G, and pmCherry-SEPT9-T339G mutants were made according to KAPA Biosystems site-directed mutagenesis protocol. Briefly, the above-mentioned SEPT9 plasmids were amplified with KAPA HiFi HotStart DNA polymerase (KAPA Biosystems) using the primers 5′-GGAGCGCATCCCCAAGGGCAT CGAGATCAAGTCC-3′ and 5′-GGACTTGATCTCGATGCCCTTGGG GATGCGCTCC-3′. The amplified PCR product was treated with DpnI (New England Biolabs) for 1 h at 37°C, heat inactivated at 80°C for 20 min, and was subsequently transformed in *Escherichia coli* DH5a-competent cells.

Expression and purification of recombinant proteins

Plasmids encoding for recombinant His-tagged proteins were transformed into *E. coli* BL21-DE3 (Invitrogen). Bacterial cultures were grown at 37°C in Luria-Bertani medium (LB) to an OD_{600} of 0.6–0.8 and induced with 0.5 mM IPTG at 18°C for 16 h (overnight). Cells were harvested by centrifugation at 4,000 rpm in a JA-10 fixed-angle rotor (Beckman Coulter). Pellets were resuspended in lysis buffer containing 50 mM Tris, pH 8, 300 mM NaCl, 10% glycerol, and 10 mM imidazole, supplemented with 2 mM PMSF (Sigma-Aldrich), a protease inhibitor cocktail (G-Biosciences), and 10 µg/ml DNase I (Millipore). Bacteria were lysed by sonication and clarified by centrifugation at 20,000 *g* for 30 min in a JA-20 rotor (Beckman) at 4°C. Supernatant was loaded onto 1 ml nickel–trichloroacetic acid (Ni-NTA) agarose beads (Macherey-Nagel), preequilibrated with 10 ml wash buffer, and rotated end over end for 1 h at 4°C. Beads were washed with 30 ml wash buffer (50 mM Tris, pH 8.0, 300 mM NaCl, 10% glycerol, 10 mM imidazole, and 2 mM PMSF) in a gravity flow column, and protein was eluted with elution buffer containing 300 mM imidazole (50 mM Tris, pH 8.0, 300 mM NaCl, 10% glycerol, 2 mM PMSF, and 300 mM imidazole). Peak fractions were combined and dialyzed overnight against 50 mM Tris, pH 8.0, 150 mM NaCl, and 10% glycerol. For proteins used in single motility assays (His-mCherry-SEPT9) and $p150^{Glued}$ CC1-Halo-6xHis, peak fractions eluted from Ni-NTA beads were further purified via size-exclusion chromatography on a Superdex 200 (GE Healthcare Life Sciences) with degassed dialysis buffer (50 mM Tris, pH 8.0, 150 mM NaCl, and 10% glycerol) at 0.5 ml/min. Peak fractions were collected and dialyzed against GF150 buffer (25 mM Hepes, pH 7.4, 150 mM KCl, 1 mM $MgCl_2$, 1 mM DTT, and 10% glycerol) overnight (Schlager et al., 2014). Proteins were aliquoted, snap frozen, and stored at −80°C. GST-tagged proteins were purified with the following modifications. Bacteria pellets were lysed in PBS containing 10% glycerol and supplemented with 2 mM PMSF (Sigma-Aldrich), a protease inhibitor cocktail (G-Biosciences), and 10 µg/ml DNase I (Millipore). Cleared lysates were loaded onto GST-Trap (GE Healthcare Life Sciences), washed with 20–30 column volumes of wash buffer (PBS, 10% glycerol, and 2 mM PMSF) at 0.5 ml/min, and eluted with 50 mM glutathione (Sigma-Aldrich; wash buffer supplemented with 50 mM glutathione). Peak fractions were dialyzed overnight against dialysis buffer (50 mM Tris, pH 8.0,

150 mM NaCl, and 10% glycerol). SEPT2/6/7 complex was expressed and purified as previously described (Nakos et al., 2019), with the modification of dialyzing the peak fraction elution from the StrepTrap HP column in buffer consisting of 50 mM Tris, pH 8.0, 150 mM NaCl, and 10% glycerol.

Dynein–dynactin purification

Native dynein/dynactin was purified from HEK-293T cells as previously described (Huynh and Vale, 2017; McKenney et al., 2014). Briefly, 10–15 plates (15 cm) were harvested per purification. Cells were washed twice with PBS and collected by scraping with a flexible blade cell scraper (VWR). Cells were pelleted at 1,000 *g* for 5 min and lysed in 2 cell-pellet volumes of Buffer A (30 mM Hepes, pH 7.4, 50 mM potassium acetate, 2 mM magnesium acetate, 1 mM EGTA, and 10% glycerol) supplemented with 2 mM PMSF, 5 mM DTT, 0.2% NP-40, and 0.1 mM ATP and a protease inhibitor cocktail (Sigma-Aldrich). Lysate was rotated end over end for 1 h at 4°C to ensure lysis. Lysate was clarified at 50,000 rpm for 30 min in a TLA 100.3 type rotor (Beckman Coulter) at 4°C. The clarified supernatant was mixed with 200 nM sfGFP-BICDN and 50 µl Streptactin beads (IBA Life Sciences) and rotated end over end overnight at 4°C. Beads were pelleted by centrifugation at 500 *g* for 1 min and washed five times with 500 µl of Buffer A supplemented with 2 mM PMSF, 5mM DTT, and 0.1% NP-40. Dynein and dynactin were eluted from superfolder GFP (sfGFP)–BICDN beads by incubating for 15 min with 50–100 µl buffer A containing 300 mM NaCl and 0.5 mM ATP on ice. The eluate was passed through a spin filter to remove any remaining beads. Eluate was diluted with two volumes of Buffer A to reduce salt concentration to 100 mM, and 6% sucrose was added before aliquoting and snap freezing.

N-terminal Strep-II sfGFP BICD2 (aa 25–400; gift from Richard McKenney, University of California, Davis, Davis, CA) was expressed in BL21-DE3 cells and purified as mentioned above with the following changes. Bacteria were lysed in Buffer A (30 mM Hepes, pH 7.4, 50 mM KoAc, 2 mM MgOAc, 1 mM EGTA, and 10% glycerol) supplemented with 2 mM PMSF, 5 mM DTT, and protease inhibitor cocktail. Clarified lysate was loaded onto a Step-Tactin column (GE Healthcare Life Sciences), washed with 20–30 column volumes of wash buffer (Buffer A, 2 mM PMSF and 5 mM DTT), and eluted with Buffer A supplemented with 5 mM DTT and 3 mM desthiobiotin (Sigma-Aldrich). Peak fractions were combined and further purified via size exclusion chromatography on a Superdex 200 (GE Healthcare Life Sciences) with degassed dialysis Buffer A supplemented with 5 mM DTT at 0.5 ml/min. Fractions corresponding to monomers/dimers of sfGFP-BICD2 (aa 25–400) were collected.

Immunoprecipitations and binding assays

GST pull-downs were performed by incubating purified GST-tagged proteins (5 µg) with 20 µl dry volume of glutathione agarose 4B beads (Thermo Fisher Scientific) for 1 h under rotation at 4°C. Beads were pelleted by centrifugation at 500 *g* for 1 min and washed three times with GST pull-down buffer (50 mM Hepes, pH 7.4, 150 mM NaCl, 2 mM EGTA, 10% glycerol, 0.1% Triton X-100, 2 mM PMSF, and 5 mM DTT) and incubated with His-tagged bait protein (5 µg) in 200 µl GST pull-down buffer under end-over-end rotation for 2 h at 4°C. Beads were washed five times with 500 µl of GST pull-down buffer and eluted in 40 µl of SDS loading buffer by boiling for 5 min. Samples (5–15 µl from the eluate) were loaded into 10% SDS-PAGE gels and stained with Coomassie Brilliant Blue (Sigma-Aldrich) or transferred to a nitrocellulose membrane. In GST pull-downs containing nucleotides, GST pull down buffer was supplemented with 10 mM $MgCl_2$.

Dynein-dynactin binding assays were performed by incubating 5 µg of His-tagged SEPT9 protein or truncations with 10 µl dry volume of Ni-NTA agarose beads (Macherey-Nagel) for 1 h under rotation at 4°C. Beads were pelleted by centrifugation at 500 *g* for 1 min and washed three times with Buffer A supplemented with 2 mM PMSF and 5 mM DTT and subsequently incubated with 20 µl of native dynein–dynactin purified from HEK-293 cells (as described above) in a total volume of 200 µl Buffer A supplemented with 2 mM PSMF, 5 mM DTT, and 0.1% NP-40. Beads were incubated under end-over-end rotation for 2 h at 4°C. Beads were pelleted and washed five times with Buffer A supplemented with 2 mM PSMF and 5 mM DTT and eluted in 20 µl of SDS loading buffer by boiling for 5 min. Samples were loaded into 6% or 10% SDS-PAGE gels and stained with Coomassie Brilliant Blue (5 µl from the eluate) or transferred to a nitrocellulose membrane (15 µl from the eluate).

For coimmunoprecipitation experiments, HEK-293T cells were plated on 10-cm dishes at ∼40% confluency the day before transfection in antibiotic-free medium. Cells were transfected with 2 µg plasmid DNA using Metafectene-PRO (Biontex) according to the manufacturer's instructions, and two plates were transfected per condition. After 6 h, medium was exchanged for complete DMEM containing 10% FBS and penicillin/streptomycin/kanamycin (PSK). Cells were grown for 24 h before lysate preparation. Cells were washed twice with ice-cold PBS and collected by scraping in lysis buffer (Buffer A supplemented with 2 mM PMSF, protease inhibitors cocktail, 5 mM DTT, and 0.2% NP-40). To ensure lysis, cells were incubated for 30 min at 4°C rotating end over end. Lysate was cleared by centrifugation at 16,000 *g* for 20 min at 4°C (Eppendorf). Supernatant was collected, and protein content was quantified by Bradford spectrophotometry (Bio-Rad). Equal micrograms of protein extracts were mixed with 20 µl of RFP trap Agarose beads, and the lysates were incubated overnight at 4°C under end-over-end rotation. Beads were washed five times with 500 µl of lysis buffer, boiled in 25 µl SDS loading buffer, and run on a 10% SDS-PAGE gel. Gels were subsequently transferred to a nitrocellulose membrane and processed for Western blotting.

Cell culture, transfections, and treatments

COS-7 (American Type Culture Collection [ATCC]: CRL-1651), HEK-293T (ATCC: CRL-3216), and HeLa-CCL2 (ATCC: CCL-2) cells were maintained in a humidified incubator 37°C with 5% CO_2 in high-glucose DMEM (Sigma-Aldrich) supplemented with 10% FBS (R&D Systems) and 1% penicillin/streptomycin/kanamycin (Sigma-Aldrich and Gibco). Primary rat embryonic (E18) hippocampal neurons were obtained from the Neuron Culture Service Center (University of Pennsylvania) and cultured in

neurobasal medium as previously described (Karasmanis et al., 2018). BSC-1 cells stably expressing GFP-tubulin and mCherry-LAMP2 (gift from Melike Lakadamyali, University of Pennsylvania, Philadelphia, PA) were maintained as described previously (Mohan et al., 2019). For immunofluorescence or live-imaging experiments, cells were seeded at a density of 70–100,000 cells on 22-mm glass coverslips or 35-mm glass-bottom dishes (MatTek) coated with 30 µg/ml type I bovine collagen (Advanced Biomatrix).

For all immunofluorescence experiments, COS-7 cells were transfected with 0.25 µg DNA using Lipofectamine 2000 for 24 h unless otherwise stated. Medium was exchanged 6 h after transfection. MitoTagRFP-septin constructs were transfected using 1 µg of DNA, and in cotransfection experiments, 0.75 µg of MitoTagRFP constructs was combined with 0.25 µg of GFP- or GFP-p50–encoding plasmids. For the inducible peroxisome trafficking assay in Fig. 2 A, cells were transfected with 0.25 µg GFP-SEPT9-FRB plasmid and 0.25 µg PEX-RFP-FKBP plasmid. Cells were induced with 1 µM rapalog (AP21967; Takara) for 45 min at 37°C. Cells in Fig. 1 L were transfected with two plasmids of equal concentration (0.25 µg each). For cotransfection experiments in Fig. S2 F, cells were transfected with 0.75 µg SEPT9 shRNA or scrambled shRNA control combined with 0.25 µg MitoTagFRP constructs and assayed 72 h after transfections. For SEPT9 depletion experiments (Fig. 1, J and K; and Fig. S1, I and J), COS-7 cells were seeded on 35-mm dishes at ∼40–60% confluency 1 d before transfection and transfected with 1 µg plasmid DNA using 3 µl of Lipofectamine. Medium was exchanged 6 h after transfection. After 48 h, cells were trypsinized and replated on 22-mm glass coverslips (80,000 cells per well). Cells were fixed and assayed 72 h after transfection. For the experiment in Fig. 5, C–E, COS-7 cells were transfected and replated as described above but with 0.5 µg DNA and 1.5 µl Lipofectamine instead of 1 µg DNA and 3 µl Lipofectamine, respectively. For SEPT9 depletion experiments in Fig. 5, F and G, and Fig. S4 C, HeLa cells were seeded on 35-mm dishes containing 22-mm glass coverslips at 60% confluency 1 d before transfection and transfected with 1 µg plasmid DNA using 3 µl of Lipofectamine. Medium was exchanged 6 h after transfection. Cells were fixed and assayed 48 h after transfection. In Fig. S4, A and B, HeLa cells were plated and transfected as described above, except they were assayed 72 h after transfection. Primary rat hippocampal neurons (2–4 days in vitro [DIV2–4]) were transfected with 0.4–0.5 µg of ratSEPT9_i1-mCherry plasmid combined with 0.4 µg of plasmid encoding LAMP1-mGFP or GFP-Rab5A using Lipofectamine 3000 (Karasmanis et al., 2018). Neurons were assayed 48 h after transfection. Nocodazole treatment was performed by incubating cells with 33 µM nocodazole (Sigma-Aldrich) for 3 h, and 0.1% vol/vol DMSO was used as vehicle control. Acute oxidative stress was induced by incubating COS-7 cells with 300 µM sodium-(meta)arsenite ($NaAsO_2$; Sigma-Aldrich) for 30 or 120 min (Willett et al., 2017) and HeLa cells with 400 µM $NaAsO_2$ for 1 h. For glucose deprivation experiments, cells were incubated in glucose-free DMEM (Gibco) containing dialyzed FBS (Gibco) for 1 h.

Immunofluorescence

Cells in Fig. 1, A and B, and Fig. 5 A were fixed with warm 2% PFA (Electron Microscopy Sciences) in PBS containing 0.4% wt/vol sucrose for 12 min at room temperature and quenched with 0.25% ammonium chloride (Sigma-Aldrich) for 10 min. Cells were simultaneously blocked and permeabilized in 0.2% porcine gelatin (Sigma-Aldrich) and 0.1% wt/vol saponin (Millipore) for 30 min at room temperature. Primary antibodies were incubated overnight at 4°C, and secondary antibodies were incubated at room temperature for 1 h in 0.2% porcine gelatin BSA and 0.1% wt/vol Saponin in PBS. Co-stains of mouse anti-SEPT9 and mouse anti-EEA1 in Fig. 1 B were performed using the Zenon Alexa Fluor 647 mouse IgG Labeling Kit (Z25008; Invitrogen), according to the manufacturer's instructions. Briefly, cells were fixed, permeabilized, blocked, and stained for SEPT9 with an anti-mouse–Alexa Fluor 488 secondary antibody as described above. Subsequently, 1 µg of mouse anti EEA1 antibody was sequentially incubated with 5 µl of the Zenon mouse IgG labeling reagent and 5 µl of Zenon mouse blocking reagent in 1× PBS for 5 min at room temperature. The complexes were further diluted in blocking buffer and incubated with the samples for 1 h at room temperature. Cells were washed with 1× PBS, mounted in FluorSave hard mounting medium (EMD Millipore-Calbiochem), and imaged immediately. Primary rat hippocampal neurons were fixed and stained as previously described (Karasmanis et al., 2018).

Cells in Fig. 1, H, J, and L; Fig. S1, E and G; Fig. 4 G; Fig. 5 C; and Fig. S4 C were fixed with warm 3% PFA (Electron Microscopy Sciences) in PBS containing 0.4% wt/vol sucrose for 15 min at room temperature and quenched with 0.25% ammonium chloride (Sigma-Aldrich) for 10 min. Cells were subsequently blocked and permeabilized with 3% BSA (Sigma-Aldrich) and 0.2% wt/vol saponin (Millipore) for 30 min at room temperature. Primary antibodies were incubated for 1 h at room temperature or overnight at 4°C in 3% BSA and 0.2% wt/vol saponin in PBS. Secondary antibodies were incubated at room temperature for 1 h in 3% BSA and 0.2% wt/vol saponin in PBS.

Cells in Fig. 1 D were fixed and stained as described previously (Mohan et al., 2019) with the following modifications. Briefly, cells were fixed with 4% PFA (Electron Microscopy Sciences) in PBS for 20 min, and 0.25% ammonium chloride (Sigma-Aldrich) was used to quench background fluorescence. Cells were blocked and simultaneously permeabilized with 3% BSA (Sigma-Aldrich) and 0.2% Triton X-100 (Sigma-Aldrich) dissolved in PBS. Cells were incubated with primary and secondary antibodies in blocking buffer and were rinsed between antibody incubation with 0.2% BSA and 0.05% Triton X-100.

Cells in Fig. 2; Fig. S2, C, E, and F; and Fig. 4, C and E, were fixed with warm 2% PFA in PBS containing 0.4% wt/vol sucrose for 12 min at room temperature and quenched with 0.25% ammonium chloride (Sigma-Aldrich) for 10 min. Cells were permeabilized in 0.1% Triton for 10 min at room temperature and blocked with 0.2% porcine gelatin in PBS. Primary antibodies were incubated overnight at 4°C, and secondary antibodies were incubated for 1 h at room temperature in 0.2% porcine gelatin in PBS.

Western blotting

Samples were loaded onto 10% or 6% SDS-PAGE gels and transferred to a 0.45-µm nitrocellulose membrane (Amersham GE Healthcare) overnight at 4°C in Tris-glycine buffer under constant voltage (30 V). Membranes were blocked with 5%

nonfat dry milk and 1% BSA in PBS for 1 h at room temperature. Membranes were washed with PBS-T (PBS/0.1% Tween 20) and incubated with primary antibodies in PBS-T buffer containing 2% BSA and 0.025% sodium azide for 2 h at room temperature or overnight at 4°C. Subsequently, membranes were washed with PBS-T and incubated with anti-mouse or anti-rabbit secondary antibodies (LI-COR) diluted in antibody dilution buffer for 1 h at room temperature before scanning with an Odyssey infrared imaging system (Odyssey; LI-COR).

Iodixanol density gradients

For membrane fractionation experiments, two subconfluent 15-cm dishes were trypsinized and washed twice with PBS. Cell pellet was resuspended in homogenization buffer (20 mM Hepes, pH 7.4, and 1 mM EDTA) supplemented with 2 mM PMSF (Sigma-Aldrich) and protease inhibitor cocktail (Sigma-Aldrich). Cells were incubated on ice for 10 min and homogenized by passing 10–15 times through a 22.5G needle. Cell breakage was confirmed microscopically by Trypan Blue stain (Sigma-Aldrich). To restore isosmotic conditions, an equal volume of homogenization buffer containing 0.5 M sucrose (Sigma-Aldrich) was added to the cell homogenate. Nuclei were pelleted by centrifugation at 1,000 *g* for 5 min at 4°C. The resulting postnuclear supernatant (PNS) was diluted in OptiPrep gradient medium to a final concentration of 15% OptiPrep (Sigma-Aldrich) in a total volume of 1.5 ml. The PNS was carefully layered on top of a discontinuous OptiPrep step gradient (17%, 20%, 23%, 27%, and 30%) prepared in descending concentrations. The gradient was centrifuged at 145,000 *g* in a SW60 Ti swinging bucket rotor (Beckman) for 2 h at 4°C. Fractions (350 µl) were collected from top to bottom.

Microscopy

Fixed samples were imaged on a Zeiss AxioObserver Z1 inverted microscope equipped with a Zeiss 20×/0.8-NA dry objective, a 40×/1.2-NA water objective, a 63×/1.4-NA oil objective, a Hamamatsu Orca-R2 charge-coupled device camera, and Slidebook 6.0 software. Fixed cells in Fig. 1, A and B, and live cells in Fig. S2 A were imaged on a laser scanning confocal microscope (LSM700; Carl Zeiss), equipped with an environmental chamber and operated by Zen software (Carl Zeiss). Optical sections were acquired according to Niquist criteria with a 63×/1.4-NA oil objective (Carl Zeiss). The PureDenoise plugin was used after acquisition to remove Poisson shot noise from confocal images (Fig. 1, A, B, and G) using an automated, global noise estimation in Fiji software.

Super-resolution structured illumination microscopy was performed for Fig. 1 D using DeltaVision OMX V4 (GE Healthcare) with an Olympus 60×/1.42-NA objective and immersion oil with a refractive index of 1.516. Images were acquired using a 0.125-µm z-step, sCMOS pco.edge camera (custom version) and reconstructed with softWoRx software (Applied Precision). Total internal reflection fluorescence (TIRF) imaging (20–60 frames/min) of live neurons was performed at 37°C using the TIRF module on the DeltaVision OMX V4 inverted microscope equipped with an Olympus 60×/1.49-NA objective and a temperature-controlled stage-top incubator.

Time-lapse imaging of COS-7 cells in Fig. 1, E and F, and Fig. S1 A was performed with an inverted Olympus IX83 spinning-disk confocal system equipped with a Yokogawa CSU 10 spinning disk, a motorized stage, solid state 405-, 488-, 561-, and 640-nm laser lines, a Hamamatsu Orca Flash 4 CMOS camera, and an environmental control chamber (Okolab). Images were acquired using a 60×/1.49-NA oil objective (Olympus) and the VisiView software. COS-7 cells were cotransfected with plasmid expressing SEPT9_i1-mCherry under the weak PGK promoter and plasmids encoding LAMP1-mGFP or GFP-EEA1. Cells were imaged 24 h after transfection at 37°C and 5% CO_2 in FluoroBrite DMEM (Gibco) supplemented with 10% FBS and 1% protein-bound polysaccharide-K. Low expressing cells were identified and imaged at 3-s intervals for a total duration of 5 min.

Live imaging of hippocampal neurons (DIV4–6) was performed 48 h after transfection with the TIRF microscopy module of the DeltaVision OMX V4 system described above, using a 60×/1.49-NA objective and temperature-controlled (37°C) environmental chamber. Cell medium was replaced with phenol red-free neurobasal medium supplemented with 2% B27 (Invitrogen) and 30 mM Hepes, and dishes were sealed using ParaFilm. Axons were identified as the longest process/neurite and imaged at 1-s intervals for a total duration of 2–4 min. Videos are displayed at the rate of 1 frame/s.

For live-cell imaging of MitoSpy-labeled cells (Fig. S2 A), cells were incubated with 50 nM MitoSpy NIR DilC1 dye for 30 min at 37°C. Cells were subsequently washed twice with imaging medium (FluoroBrite DMEM; Gibco) and imaged with the Zeiss LSM700 confocal laser-scanning microscopy in an environmental chamber (37°C, 5% CO_2).

Image analysis and quantifications

All image processing and quantitative analyses were performed with the open-source software Fiji. Ratios of perinuclear to peripheral fluorescence intensity were derived by dividing the mean perinuclear intensity by the mean peripheral intensity using the formula $(I_{Perinuclear} - BG/area_{Perinuclear})/[(I_{Total} - BG) - (I_{Perinuclear} - BG)]/(area_{Total} - area_{Perinuclear})$, with I denoting mean fluorescence intensity and BG corresponding to mean background intensity. Perinuclear area was defined as the area contained within a 40-µm-diameter circle positioned around the cell nucleus. Sum intensities for each area were measured, and background was subtracted. Mean background intensity was measured by quantifying fluorescence intensity in a circular extracellular region and multiplying it by a factor equal to total cell or perinuclear surface area under quantification. Cell perimeter was traced manually using the freehand selection tool.

Cumulative lysosome intensity was measured and plotted as recently described (Starling et al., 2016). Cell perimeter was defined by thresholding GFP fill expressed from shRNA plasmids and corrected manually where necessary using the freehand selection tool. Cell area was scaled in 10% decrements, and sum intensity (integrated density) was measured for each decrease. Background was subtracted using the subtract background function in Fiji (rolling ball radius = 50). Intensity of each fraction was normalized by dividing by the total cell intensity. Cumulative LAMP-1 intensity was plotted against the respective

cell fraction. Curves were fitted using nonlinear regression, second-order polynomial being the preferred fitting model for our data. Statistical significance between different fitting models and different experimental conditions was assessed using the extra sum of squares *F* test.

The ratio of retrograde to anterograde motility in neurons was derived by dividing the number of retrograde motility events of mCherry- or mCherry-SEPT9–positive Lamp1 vesicles by the number of anterograde motility events per axon, per 2 min of time-lapse video. Each axon was imaged once.

Percentage intensity of perinuclear mitochondria was derived by dividing the sum perinuclear intensity by the sum cell intensity using the formula $[(I_{Perinuclear} - BG)/(I_{Total} - BG)] \times 100$. Percentage peripheral intensity was calculated by subtracting perinuclear intensity from 100. Perinuclear area was defined as the area contained within a 40-µm-diameter circle positioned around the cell nucleus. Mean background intensity was measured by drawing a circular extracellular area and multiplying it by a factor equal to total cell or perinuclear area and considered background intensity (BG). Cell perimeter was traced manually using the freehand selection tool.

Percentages of EEA1- and LAMP1-positive organelles with SEPT9 (Figs. 1 C and S1 L) were quantified in COS7 cell and neuronal axon images after applying a median filter. Puncta with signal above background levels and a >30% surface area overlap with membrane marker were scored as positive. Percentage of SEPT9-positive organelles was calculated by dividing the number of SEPT9-positive by the total number of organelles per cell, multiplied by 100. In Fig. 1 C, lysosomes in contact with septin filaments were not included in the quantification. In Fig. 1 D, single lysosomes were volume rendered in 3D using the 3D viewer plugin of Fiji software. In Fig. S1 B, the percentage of mCherry-SEPT9_i1 puncta that overlapped with LAMP1-mGFP or GFP-EEA1 was calculated in Fiji by creating masks of mCherry-SEPT9_i1 puncta in the 594-nm channel and overlaying them with LAMP1-mGFP or GFP-EEA1. Nonoverlapping puncta were deleted using the DeleteSelected_ROI2 macro created by Kees Straatman (University of Leicester, Leicester, UK), and overlapping puncta were counted as percentage of total per cell. This quantification was performed in the first frame of the time-lapse series acquired by spinning-disk confocal microscopy. Images in Fig. 1, E and F; Fig. S1 A; and Video 1 were bleach corrected in Fiji (histogram matching).

Quantification of the fluorescence intensity of DIC (Figs. 2 E and 4 F) or MitoSpy dye (Fig. S2 A) in the mitochondria channel was processed in Fiji with a fast Fourier transform–based bandpass filter to eliminate noise (Giedt et al., 2016), and mitochondria masks were subsequently created using an autothreshold algorithm. Fluorescence DIC or MitoSpy intensity was measured in the mitochondria masks. Background subtraction was performed with the rolling ball background subtraction tool using a ∼50-pixel averaging subtraction ball.

In Fig. 5 B, SEPT9-LAMTOR4 overlap was quantified by creating masks that correspond to SEPT9 and LAMTOR4 signal intensities, and an overlap mask was derived and corrected using the watershed separation algorithm. The surface area (µm^2) of each overlap and LAMTOR4 mask and the percentage of overlap per cell was derived by dividing the total surface area of the overlap masks by the total surface area of LAMTOR4 and multiplying by 100. Masks were created from thresholded images after applying a Laplacian filter followed by Gaussian blur filtering (2-σ radius). Background was subtracted using rolling ball background subtraction (50-pixel ball radius).

Quantification of SEPT9 depletion (Figs. S1 J and S4 B) was performed in images of SEPT9-stained cells transfected with scrambled and SEPT9 shRNAs. Cell periphery was outlined manually using free-hand selection using the GFP signal from the pGFP-Super expressing plasmids as a guide. Background was subtracted using a round region of interest at the extracellular area close to the cell of interest. In Fig. 1 G, color-coded trajectory was generated by computing maximum projections of time series every four frames and subsequently making three-color overlays. The SEPT9-mCherry signal was used to follow the trajectory of SEPT9-positive Lamp1 endolysosomes. All Western blots and Coomassie-stained gels were quantified in Image Studio Lite (Odyssey; LI-COR), and background was subtracted using the median background method.

Statistical analysis

Statistics were performed in GraphPad Prism 5.0. Datasets were tested for normal distribution or variance using the D'Agostino and Pearson normality test. Data exhibiting normal distribution were tested using Student's *t* test when comparing two datasets, while one-way ANOVA with Bonferroni post hoc test was used when comparing multiple datasets. For non–normally distributed data, a Mann-Whitney *U* test was used when comparing two datasets, and a Kruskal–Wallis test with Dunn's multiple comparison test was used when comparing multiple datasets. Two-way ANOVA with Bonferroni post hoc test was used when comparing grouped datasets. Qualitatively binned datasets were analyzed using χ^2 test. All graphs were generated in GraphPad Prism 5.0.

Online supplemental material

Fig. S1 shows the specificity of the localization and effects of SEPT9 on lysosomes. Fig. S2 shows the localization of mitochondria and endogenous septin paralogs in cells that express mitochondria-targeted septins and the SEPT9 dependency of the perinuclear clustering phenotype. Fig. S3 shows that SEPT2/6/7 does not interact with DIC(108–268). Fig. S4 shows that SEPT9 is required for the perinuclear accumulation of lysosomes in HeLa cells undergoing acute oxidative stress. Video 1 shows cotrafficking of SEPT9_i1-mCherry with LAMP1-mGFP in COS-7 cells. Video 2 shows LAMP1-mGFP traffic in the axon of a rat embryonic hippocampal neuron (DIV4) that expresses mCherry. Video 3 shows LAMP1-mGFP traffic in the axon of a rat embryonic hippocampal neuron (DIV4) that expresses rat SEPT9_i1-mCherry.

Acknowledgments

We thank Drs. Erika Holzbaur (University of Pennsylvania, Philadelphia, PA), Adam Kwiatkowski (University of Pittsburgh, Pittsburgh, PA), Melike Lakadamyali (University of Pennsylvania),

Trina Schroer (The Johns Hopkins University, Baltimore, MD), and Zu-Hang Sheng (National Institutes of Health, Bethesda, MD) for donating constructs and helpful advice. We are grateful to Dr. Sam Reck-Peterson and John Gillies (University of California San Diego, Howard Hughes Medical Institute, La Jolla, CA) for in vitro motility assays of dynein activation. We also acknowledge Megan Radler, Brenna Doyle, and Drs. Konstantinos Nakos and Eva Karasmanis for help and feedback on the manuscript. All microscopy was performed in Drexel University's Cell Imaging Center.

This work was supported with National Institutes of Health/National Institute of General Medical Sciences grants RO1 GM097664 and R35 GM136337 to E.T. Spiliotis.

The authors declare no competing financial interests.

Author contributions: I.A. Kesisova designed and performed the majority of the experiments, analyzed data, and assembled figures. B.P. Robinson performed experiments and analyzed data. E.T. Spiliotis initiated and directed the study and wrote the manuscript with feedback from I.A. Kesisova.

Submitted: 1 June 2020
Revised: 22 November 2020
Accepted: 9 December 2020

References

Akil, A., J. Peng, M. Omrane, C. Gondeau, C. Desterke, M. Marin, H. Tronchère, C. Taveneau, S. Sar, P. Briolotti, et al. 2016. Septin 9 induces lipid droplets growth by a phosphatidylinositol-5-phosphate and microtubule-dependent mechanism hijacked by HCV. *Nat. Commun.* 7:12203. https://doi.org/10.1038/ncomms12203

Andrews, N.W., and M. Corrotte. 2018. Plasma membrane repair. *Curr. Biol.* 28:R392–R397. https://doi.org/10.1016/j.cub.2017.12.034

Ayloo, S., J.E. Lazarus, A. Dodda, M. Tokito, E.M. Ostap, and E.L. Holzbaur. 2014. Dynactin functions as both a dynamic tether and brake during dynein-driven motility. *Nat. Commun.* 5:4807. https://doi.org/10.1038/ncomms5807

Bai, X., J.R. Bowen, T.K. Knox, K. Zhou, M. Pendziwiat, G. Kuhlenbäumer, C.V. Sindelar, and E.T. Spiliotis. 2013. Novel septin 9 repeat motifs altered in neuralgic amyotrophy bind and bundle microtubules. *J. Cell Biol.* 203:895–905. https://doi.org/10.1083/jcb.201308068

Bai, X., E.P. Karasmanis, and E.T. Spiliotis. 2016. Septin 9 interacts with kinesin KIF17 and interferes with the mechanism of NMDA receptor cargo binding and transport. *Mol. Biol. Cell.* 27:897–906. https://doi.org/10.1091/mbc.E15-07-0493

Blott, E.J., and G.M. Griffiths. 2002. Secretory lysosomes. *Nat. Rev. Mol. Cell Biol.* 3:122–131. https://doi.org/10.1038/nrm732

Bonifacino, J.S., and J. Neefjes. 2017. Moving and positioning the endolysosomal system. *Curr. Opin. Cell Biol.* 47:1–8. https://doi.org/10.1016/j.ceb.2017.01.008

Bowen, J.R., D. Hwang, X. Bai, D. Roy, and E.T. Spiliotis. 2011. Septin GTPases spatially guide microtubule organization and plus end dynamics in polarizing epithelia. *J. Cell Biol.* 194:187–197. https://doi.org/10.1083/jcb.201102076

Bridges, A.A., and A.S. Gladfelter. 2015. Septin Form and Function at the Cell Cortex. *J. Biol. Chem.* 290:17173–17180. https://doi.org/10.1074/jbc.R114.634444

Burkhardt, J.K., C.J. Echeverri, T. Nilsson, and R.B. Vallee. 1997. Overexpression of the dynamitin (p50) subunit of the dynactin complex disrupts dynein-dependent maintenance of membrane organelle distribution. *J. Cell Biol.* 139:469–484. https://doi.org/10.1083/jcb.139.2.469

Castro, D.K.S.D.V., S.M.O. da Silva, H.D. Pereira, J.N.A. Macedo, D.A. Leonardo, N.F. Valadares, P.S. Kumagai, J. Brandão-Neto, A.P.U. Araújo, and R.C. Garratt. 2020. A complete compendium of crystal structures for the human SEPT3 subgroup reveals functional plasticity at a specific septin interface. *IUCrJ.* 7:462–479. https://doi.org/10.1107/S2052252520002973

Castro-Castro, A., V. Marchesin, P. Monteiro, C. Lodillinsky, C. Rossé, and P. Chavrier. 2016. Cellular and Molecular Mechanisms of MT1-MMP-Dependent Cancer Cell Invasion. *Annu. Rev. Cell Dev. Biol.* 32:555–576. https://doi.org/10.1146/annurev-cellbio-111315-125227

Caudron, F., and Y. Barral. 2009. Septins and the lateral compartmentalization of eukaryotic membranes. *Dev. Cell.* 16:493–506. https://doi.org/10.1016/j.devcel.2009.04.003

Caviston, J.P., J.L. Ross, S.M. Antony, M. Tokito, and E.L. Holzbaur. 2007. Huntingtin facilitates dynein/dynactin-mediated vesicle transport. *Proc. Natl. Acad. Sci. USA.* 104:10045–10050. https://doi.org/10.1073/pnas.0610628104

Cella Zanacchi, F., C. Manzo, R. Magrassi, N.D. Derr, and M. Lakadamyali. 2019. Quantifying Protein Copy Number in Super Resolution Using an Imaging-Invariant Calibration. *Biophys. J.* 116:2195–2203. https://doi.org/10.1016/j.bpj.2019.04.026

Chen, T.Y., T.C. Lin, P.L. Kuo, Z.R. Chen, H.L. Cheng, Y.Y. Chao, J.S. Syu, F.I. Lu, and C.Y. Wang. 2020. Septin 7 is a centrosomal protein that ensures S phase entry and microtubule nucleation by maintaining the abundance of $p150^{glued}$. *J. Cell. Physiol.*:jcp.30037. https://doi.org/10.1002/jcp.30037

Chowdhury, S., S.A. Ketcham, T.A. Schroer, and G.C. Lander. 2015. Structural organization of the dynein–dynactin complex bound to microtubules. *Nat. Struct. Mol. Biol.* 22:345–347. https://doi.org/10.1038/nsmb.2996

Connolly, D., Z. Yang, M. Castaldi, N. Simmons, M.H. Oktay, S. Coniglio, M.J. Fazzari, P. Verdier-Pinard, and C. Montagna. 2011. Septin 9 isoform expression, localization and epigenetic changes during human and mouse breast cancer progression. *Breast Cancer Res.* 13:R76. https://doi.org/10.1186/bcr2924

Cross, J.A., and M.P. Dodding. 2019. Motor-cargo adaptors at the organelle-cytoskeleton interface. *Curr. Opin. Cell Biol.* 59:16–23. https://doi.org/10.1016/j.ceb.2019.02.010

Culver-Hanlon, T.L., S.A. Lex, A.D. Stephens, N.J. Quintyne, and S.J. King. 2006. A microtubule-binding domain in dynactin increases dynein processivity by skating along microtubules. *Nat. Cell Biol.* 8:264–270. https://doi.org/10.1038/ncb1370

Di Giovanni, J., and Z.H. Sheng. 2015. Regulation of synaptic activity by snapin-mediated endolysosomal transport and sorting. *EMBO J.* 34:2059–2077. https://doi.org/10.15252/embj.201591125

Dolat, L., and E.T. Spiliotis. 2016. Septins promote macropinosome maturation and traffic to the lysosome by facilitating membrane fusion. *J. Cell Biol.* 214:517–527. https://doi.org/10.1083/jcb.201603030

Dolat, L., J.L. Hunyara, J.R. Bowen, E.P. Karasmanis, M. Elgawly, V.E. Galkin, and E.T. Spiliotis. 2014. Septins promote stress fiber-mediated maturation of focal adhesions and renal epithelial motility. *J. Cell Biol.* 207:225–235. https://doi.org/10.1083/jcb.201405050

Ellinsworth, D.C. 2015. Arsenic, reactive oxygen, and endothelial dysfunction. *J. Pharmacol. Exp. Ther.* 353:458–464. https://doi.org/10.1124/jpet.115.223289

Estey, M.P., C. Di Ciano-Oliveira, C.D. Froese, M.T. Bejide, and W.S. Trimble. 2010. Distinct roles of septins in cytokinesis: SEPT9 mediates midbody abscission. *J. Cell Biol.* 191:741–749. https://doi.org/10.1083/jcb.201006031

Falcón-Pérez, J.M., R. Nazarian, C. Sabatti, and E.C. Dell'Angelica. 2005. Distribution and dynamics of Lamp1-containing endocytic organelles in fibroblasts deficient in BLOC-3. *J. Cell Sci.* 118:5243–5255. https://doi.org/10.1242/jcs.02633

Farías, G.G., C.M. Guardia, R. De Pace, D.J. Britt, and J.S. Bonifacino. 2017. BORC/kinesin-1 ensemble drives polarized transport of lysosomes into the axon. *Proc. Natl. Acad. Sci. USA.* 114:E2955–E2964. https://doi.org/10.1073/pnas.1616363114

Feng, Q., A.M. Gicking, and W.O. Hancock. 2020. Dynactin p150 promotes processive motility of DDB complexes by minimizing diffusional behavior of dynein. *Mol. Biol. Cell.* 31:782–792. https://doi.org/10.1091/mbc.E19-09-0495

Fu, M.M., and E.L. Holzbaur. 2013. JIP1 regulates the directionality of APP axonal transport by coordinating kinesin and dynein motors. *J. Cell Biol.* 202:495–508. https://doi.org/10.1083/jcb.201302078

Gama, J.B., C. Pereira, P.A. Simões, R. Celestino, R.M. Reis, D.J. Barbosa, H.R. Pires, C. Carvalho, J. Amorim, A.X. Carvalho, et al. 2017. Molecular mechanism of dynein recruitment to kinetochores by the Rod-Zw10-Zwilch complex and Spindly. *J. Cell Biol.* 216:943–960. https://doi.org/10.1083/jcb.201610108

Garcia, G. III, A. Bertin, Z. Li, Y. Song, M.A. McMurray, J. Thorner, and E. Nogales. 2011. Subunit-dependent modulation of septin assembly: budding yeast septin Shs1 promotes ring and gauze formation. *J. Cell Biol.* 195:993–1004. https://doi.org/10.1083/jcb.201107123

Giedt, R.J., P. Fumene Feruglio, D. Pathania, K.S. Yang, A. Kilcoyne, C. Vinegoni, T.J. Mitchison, and R. Weissleder. 2016. Computational imaging reveals mitochondrial morphology as a biomarker of cancer phenotype and drug response. *Sci. Rep.* 6:32985. https://doi.org/10.1038/srep32985

Gonzalez, M.E., O. Makarova, E.A. Peterson, L.M. Privette, and E.M. Petty. 2009. Up-regulation of SEPT9_v1 stabilizes c-Jun-N-terminal kinase and contributes to its pro-proliferative activity in mammary epithelial cells. *Cell. Signal.* 21:477–487. https://doi.org/10.1016/j.cellsig.2008.11.007

Graham, N.A., M. Tahmasian, B. Kohli, E. Komisopoulou, M. Zhu, I. Vivanco, M.A. Teitell, H. Wu, A. Ribas, R.S. Lo, et al. 2012. Glucose deprivation activates a metabolic and signaling amplification loop leading to cell death. *Mol. Syst. Biol.* 8:589. https://doi.org/10.1038/msb.2012.20

Guardia, C.M., G.G. Farías, R. Jia, J. Pu, and J.S. Bonifacino. 2016. BORC Functions Upstream of Kinesins 1 and 3 to Coordinate Regional Movement of Lysosomes along Different Microtubule Tracks. *Cell Reports.* 17: 1950–1961. https://doi.org/10.1016/j.celrep.2016.10.062

Hendricks, A.G., J.E. Lazarus, E. Perlson, M.K. Gardner, D.J. Odde, Y.E. Goldman, and E.L. Holzbaur. 2012. Dynein tethers and stabilizes dynamic microtubule plus ends. *Curr. Biol.* 22:632–637. https://doi.org/10.1016/j.cub.2012.02.023

Hoogenraad, C.C., P. Wulf, N. Schiefermeier, T. Stepanova, N. Galjart, J.V. Small, F. Grosveld, C.I. de Zeeuw, and A. Akhmanova. 2003. Bicaudal D induces selective dynein-mediated microtubule minus end-directed transport. *EMBO J.* 22:6004–6015. https://doi.org/10.1093/emboj/cdg592

Hu, W., H. Chan, L. Lu, K.T. Wong, S.H. Wong, M.X. Li, Z.G. Xiao, C.H. Cho, T. Gin, M.T.V. Chan, et al. 2020. Autophagy in intracellular bacterial infection. *Semin. Cell Dev. Biol.* 101:41–50. https://doi.org/10.1016/j.semcdb.2019.07.014

Huynh, W., and R.D. Vale. 2017. Disease-associated mutations in human BICD2 hyperactivate motility of dynein–dynactin. *J. Cell Biol.* 216: 3051–3060. https://doi.org/10.1083/jcb.201703201

Kapitein, L.C., M.A. Schlager, W.A. van der Zwan, P.S. Wulf, N. Keijzer, and C.C. Hoogenraad. 2010. Probing intracellular motor protein activity using an inducible cargo trafficking assay. *Biophys. J.* 99:2143–2152. https://doi.org/10.1016/j.bpj.2010.07.055

Karasmanis, E.P., D. Hwang, K. Nakos, J.R. Bowen, D. Angelis, and E.T. Spiliotis. 2019. A Septin Double Ring Controls the Spatiotemporal Organization of the ESCRT Machinery in Cytokinetic Abscission. *Curr. Biol.* 29:2174–2182.e7. https://doi.org/10.1016/j.cub.2019.05.050

Karasmanis, E.P., C.T. Phan, D. Angelis, I.A. Kesisova, C.C. Hoogenraad, R.J. McKenney, and E.T. Spiliotis. 2018. Polarity of Neuronal Membrane Traffic Requires Sorting of Kinesin Motor Cargo during Entry into Dendrites by a Microtubule-Associated Septin. *Dev. Cell.* 46:204–218.e7. https://doi.org/10.1016/j.devcel.2018.06.013

Kaushik, S., A.C. Massey, and A.M. Cuervo. 2006. Lysosome membrane lipid microdomains: novel regulators of chaperone-mediated autophagy. *EMBO J.* 25:3921–3933. https://doi.org/10.1038/sj.emboj.7601283

Kim, M.S., C.D. Froese, M.P. Estey, and W.S. Trimble. 2011. SEPT9 occupies the terminal positions in septin octamers and mediates polymerization-dependent functions in abscission. *J. Cell Biol.* 195:815–826. https://doi.org/10.1083/jcb.201106131

King, S.J., and T.A. Schroer. 2000. Dynactin increases the processivity of the cytoplasmic dynein motor. *Nat. Cell Biol.* 2:20–24. https://doi.org/10.1038/71338

Kinoshita, M., S. Kumar, A. Mizoguchi, C. Ide, A. Kinoshita, T. Haraguchi, Y. Hiraoka, and M. Noda. 1997. Nedd5, a mammalian septin, is a novel cytoskeletal component interacting with actin-based structures. *Genes Dev.* 11:1535–1547. https://doi.org/10.1101/gad.11.12.1535

Krokowski, S., D. Lobato-Márquez, A. Chastanet, P.M. Pereira, D. Angelis, D. Galea, G. Larrouy-Maumus, R. Henriques, E.T. Spiliotis, R. Carballido-López, and S. Mostowy. 2018. Septins Recognize and Entrap Dividing Bacterial Cells for Delivery to Lysosomes. *Cell Host Microbe.* 24: 866–874.e4. https://doi.org/10.1016/j.chom.2018.11.005

Krtková, J., M. Benáková, and K. Schwarzerová. 2016. Multifunctional Microtubule-Associated Proteins in Plants. *Front. Plant Sci.* 7:474. https://doi.org/10.3389/fpls.2016.00474

Lawe, D.C., V. Patki, R. Heller-Harrison, D. Lambright, and S. Corvera. 2000. The FYVE domain of early endosome antigen 1 is required for both phosphatidylinositol 3-phosphate and Rab5 binding. Critical role of this dual interaction for endosomal localization. *J. Biol. Chem.* 275: 3699–3705. https://doi.org/10.1074/jbc.275.5.3699

Lawrence, R.E., and R. Zoncu. 2019. The lysosome as a cellular centre for signalling, metabolism and quality control. *Nat. Cell Biol.* 21:133–142. https://doi.org/10.1038/s41556-018-0244-7

Lee, I.G., M.A. Olenick, M. Boczkowska, C. Franzini-Armstrong, E.L.F. Holzbaur, and R. Dominguez. 2018. A conserved interaction of the dynein light intermediate chain with dynein–dynactin effectors necessary for processivity. *Nat. Commun.* 9:986. https://doi.org/10.1038/s41467-018-03412-8

Lettau, M., H. Schmidt, D. Kabelitz, and O. Janssen. 2007. Secretory lysosomes and their cargo in T and NK cells. *Immunol. Lett.* 108:10–19. https://doi.org/10.1016/j.imlet.2006.10.001

Li, P., M. Gu, and H. Xu. 2019. Lysosomal Ion Channels as Decoders of Cellular Signals. *Trends Biochem. Sci.* 44:110–124. https://doi.org/10.1016/j.tibs.2018.10.006

Li, X., N. Rydzewski, A. Hider, X. Zhang, J. Yang, W. Wang, Q. Gao, X. Cheng, and H. Xu. 2016. A molecular mechanism to regulate lysosome motility for lysosome positioning and tubulation. *Nat. Cell Biol.* 18:404–417. https://doi.org/10.1038/ncb3324

Ligon, L.A., S. Karki, M. Tokito, and E.L. Holzbaur. 2001. Dynein binds to beta-catenin and may tether microtubules at adherens junctions. *Nat. Cell Biol.* 3:913–917. https://doi.org/10.1038/ncb1001-913

Lim, C.Y., and R. Zoncu. 2016. The lysosome as a command-and-control center for cellular metabolism. *J. Cell Biol.* 214:653–664. https://doi.org/10.1083/jcb.201607005

Lindén, M., B.D. Nelson, and J.F. Leterrier. 1989. The specific binding of the microtubule-associated protein 2 (MAP2) to the outer membrane of rat brain mitochondria. *Biochem. J.* 261:167–173. https://doi.org/10.1042/bj2610167

Liu, Y., X.D. Song, W. Liu, T.Y. Zhang, and J. Zuo. 2003. Glucose deprivation induces mitochondrial dysfunction and oxidative stress in PC12 cell line. *J. Cell. Mol. Med.* 7:49–56. https://doi.org/10.1111/j.1582-4934.2003.tb00202.x

Luzio, J.P., P.R. Pryor, and N.A. Bright. 2007. Lysosomes: fusion and function. *Nat. Rev. Mol. Cell Biol.* 8:622–632. https://doi.org/10.1038/nrm2217

Maldonado-Báez, L., N.B. Cole, H. Krämer, and J.G. Donaldson. 2013. Microtubule-dependent endosomal sorting of clathrin-independent cargo by Hook1. *J. Cell Biol.* 201:233–247. https://doi.org/10.1083/jcb.201208172

Matsushita, M., S. Tanaka, N. Nakamura, H. Inoue, and H. Kanazawa. 2004. A novel kinesin-like protein, KIF1Bbeta3 is involved in the movement of lysosomes to the cell periphery in non-neuronal cells. *Traffic.* 5:140–151. https://doi.org/10.1111/j.1600-0854.2003.00165.x

McKenney, R.J., W. Huynh, M.E. Tanenbaum, G. Bhabha, and R.D. Vale. 2014. Activation of cytoplasmic dynein motility by dynactin-cargo adapter complexes. *Science.* 345:337–341. https://doi.org/10.1126/science.1254198

Mohan, N., E.M. Sorokina, I.V. Verdeny, A.S. Alvarez, and M. Lakadamyali. 2019. Detyrosinated microtubules spatially constrain lysosomes facilitating lysosome-autophagosome fusion. *J. Cell Biol.* 218:632–643. https://doi.org/10.1083/jcb.201807124

Mostowy, S., and P. Cossart. 2012. Septins: the fourth component of the cytoskeleton. *Nat. Rev. Mol. Cell Biol.* 13:183–194. https://doi.org/10.1038/nrm3284

Mostowy, S., M. Bonazzi, M.A. Hamon, T.N. Tham, A. Mallet, M. Lelek, E. Gouin, C. Demangel, R. Brosch, C. Zimmer, et al. 2010. Entrapment of intracytosolic bacteria by septin cage-like structures. *Cell Host Microbe.* 8:433–444. https://doi.org/10.1016/j.chom.2010.10.009

Nakos, K., M.R. Radler, and E.T. Spiliotis. 2019. Septin 2/6/7 complexes tune microtubule plus-end growth and EB1 binding in a concentration- and filament-dependent manner. *Mol. Biol. Cell.* 30:2913–2928. https://doi.org/10.1091/mbc.E19-07-0362

Olenick, M.A., and E.L.F. Holzbaur. 2019. Dynein activators and adaptors at a glance. *J. Cell Sci.* 132:jcs227132. https://doi.org/10.1242/jcs.227132

Omrane, M., A.S. Camara, C. Taveneau, N. Benzoubir, T. Tubiana, J. Yu, R. Guérois, D. Samuel, B. Goud, C. Poüs, et al. 2019. Septin 9 has Two Polybasic Domains Critical to Septin Filament Assembly and Golgi Integrity. *iScience.* 13:138–153. https://doi.org/10.1016/j.isci.2019.02.015

Pankiv, S., E.A. Alemu, A. Brech, J.A. Bruun, T. Lamark, A. Overvatn, G. Bjørkøy, and T. Johansen. 2010. FYCO1 is a Rab7 effector that binds to LC3 and PI3P to mediate microtubule plus end-directed vesicle transport. *J. Cell Biol.* 188:253–269. https://doi.org/10.1083/jcb.200907015

Progida, C., L. Malerød, S. Stuffers, A. Brech, C. Bucci, and H. Stenmark. 2007. RILP is required for the proper morphology and function of late endosomes. *J. Cell Sci.* 120:3729–3737. https://doi.org/10.1242/jcs.017301

Progida, C., M.R. Spinosa, A. De Luca, and C. Bucci. 2006. RILP interacts with the VPS22 component of the ESCRT-II complex. *Biochem. Biophys. Res. Commun.* 347:1074–1079. https://doi.org/10.1016/j.bbrc.2006.07.007

Quintyne, N.J., S.R. Gill, D.M. Eckley, C.L. Crego, D.A. Compton, and T.A. Schroer. 1999. Dynactin is required for microtubule anchoring at centrosomes. *J. Cell Biol.* 147:321–334. https://doi.org/10.1083/jcb.147.2.321

Rai, A., D. Pathak, S. Thakur, S. Singh, A.K. Dubey, and R. Mallik. 2016. Dynein Clusters into Lipid Microdomains on Phagosomes to Drive Rapid Transport toward Lysosomes. *Cell.* 164:722–734. https://doi.org/10.1016/j.cell.2015.12.054

Reck-Peterson, S.L., W.B. Redwine, R.D. Vale, and A.P. Carter. 2018. The cytoplasmic dynein transport machinery and its many cargoes. *Nat. Rev. Mol. Cell Biol.* 19:382–398. https://doi.org/10.1038/s41580-018-0004-3

Redwine, W.B., M.E. DeSantis, I. Hollyer, Z.M. Htet, P.T. Tran, S.K. Swanson, L. Florens, M.P. Washburn, and S.L. Reck-Peterson. 2017. The human cytoplasmic dynein interactome reveals novel activators of motility. *eLife.* 6:e28257. https://doi.org/10.7554/eLife.28257

Rocha, N., C. Kuijl, R. van der Kant, L. Janssen, D. Houben, H. Janssen, W. Zwart, and J. Neefjes. 2009. Cholesterol sensor ORP1L contacts the ER protein VAP to control Rab7-RILP-p150 Glued and late endosome positioning. *J. Cell Biol.* 185:1209–1225. https://doi.org/10.1083/jcb.200811005

Rosa-Ferreira, C., and S. Munro. 2011. Arl8 and SKIP act together to link lysosomes to kinesin-1. *Dev. Cell.* 21:1171–1178. https://doi.org/10.1016/j.devcel.2011.10.007

Saftig, P., and J. Klumperman. 2009. Lysosome biogenesis and lysosomal membrane proteins: trafficking meets function. *Nat. Rev. Mol. Cell Biol.* 10:623–635. https://doi.org/10.1038/nrm2745

Savini, M., Q. Zhao, and M.C. Wang. 2019. Lysosomes: Signaling Hubs for Metabolic Sensing and Longevity. *Trends Cell Biol.* 29:876–887. https://doi.org/10.1016/j.tcb.2019.08.008

Schlager, M.A., H.T. Hoang, L. Urnavicius, S.L. Bullock, and A.P. Carter. 2014. In vitro reconstitution of a highly processive recombinant human dynein complex. *EMBO J.* 33:1855–1868. https://doi.org/10.15252/embj.201488792

Schmidt, H., and A.P. Carter. 2016. Review: Structure and mechanism of the dynein motor ATPase. *Biopolymers.* 105:557–567. https://doi.org/10.1002/bip.22856

Schroeder, C.M., and R.D. Vale. 2016. Assembly and activation of dynein–dynactin by the cargo adaptor protein Hook3. *J. Cell Biol.* 214:309–318. https://doi.org/10.1083/jcb.201604002

Schroeder, C.M., J.M. Ostrem, N.T. Hertz, and R.D. Vale. 2014. A Ras-like domain in the light intermediate chain bridges the dynein motor to a cargo-binding region. *eLife.* 3:e03351. https://doi.org/10.7554/eLife.03351

Schroer, T.A. 2004. Dynactin. *Annu. Rev. Cell Dev. Biol.* 20:759–779. https://doi.org/10.1146/annurev.cellbio.20.012103.094623

Schroer, T.A., and M.P. Sheetz. 1991. Two activators of microtubule-based vesicle transport. *J. Cell Biol.* 115:1309–1318. https://doi.org/10.1083/jcb.115.5.1309

Schwake, M., B. Schröder, and P. Saftig. 2013. Lysosomal membrane proteins and their central role in physiology. *Traffic.* 14:739–748. https://doi.org/10.1111/tra.12056

Sellin, M.E., L. Sandblad, S. Stenmark, and M. Gullberg. 2011. Deciphering the rules governing assembly order of mammalian septin complexes. *Mol. Biol. Cell.* 22:3152–3164. https://doi.org/10.1091/mbc.e11-03-0253

Senoo, H., Y. Kamimura, R. Kimura, A. Nakajima, S. Sawai, H. Sesaki, and M. Iijima. 2019. Phosphorylated Rho-GDP directly activates mTORC2 kinase towards AKT through dimerization with Ras-GTP to regulate cell migration. *Nat. Cell Biol.* 21:867–878. https://doi.org/10.1038/s41556-019-0348-8

Settembre, C., A. Fraldi, D.L. Medina, and A. Ballabio. 2013. Signals from the lysosome: a control centre for cellular clearance and energy metabolism. *Nat. Rev. Mol. Cell Biol.* 14:283–296. https://doi.org/10.1038/nrm3565

Sirajuddin, M., M. Farkasovsky, E. Zent, and A. Wittinghofer. 2009. GTP-induced conformational changes in septins and implications for function. *Proc. Natl. Acad. Sci. USA.* 106:16592–16597. https://doi.org/10.1073/pnas.0902858106

Sirianni, A., S. Krokowski, D. Lobato-Márquez, S. Buranyi, J. Pfanzelter, D. Galea, A. Willis, S. Culley, R. Henriques, G. Larrouy-Maumus, et al. 2016. Mitochondria mediate septin cage assembly to promote autophagy of Shigella. *EMBO Rep.* 17:1029–1043. https://doi.org/10.15252/embr.201541832

Song, K., G. Russo, and M. Krauss. 2016. Septins As Modulators of Endo-Lysosomal Membrane Traffic. *Front. Cell Dev. Biol.* 4:124. https://doi.org/10.3389/fcell.2016.00124

Song, S.B., and E.S. Hwang. 2018. A Rise in ATP, ROS, and Mitochondrial Content upon Glucose Withdrawal Correlates with a Dysregulated Mitochondria Turnover Mediated by the Activation of the Protein Deacetylase SIRT1. *Cells.* 8:11. https://doi.org/10.3390/cells8010011

Spiliotis, E.T. 2018. Spatial effects - site-specific regulation of actin and microtubule organization by septin GTPases. *J. Cell Sci.* 131:jcs207555. https://doi.org/10.1242/jcs.207555

Starling, G.P., Y.Y. Yip, A. Sanger, P.E. Morton, E.R. Eden, and M.P. Dodding. 2016. Folliculin directs the formation of a Rab34-RILP complex to control the nutrient-dependent dynamic distribution of lysosomes. *EMBO Rep.* 17:823–841. https://doi.org/10.15252/embr.201541382

Sun, Q., W. Westphal, K.N. Wong, I. Tan, and Q. Zhong. 2010. Rubicon controls endosome maturation as a Rab7 effector. *Proc. Natl. Acad. Sci. USA.* 107:19338–19343. https://doi.org/10.1073/pnas.1010554107

Sweeney, H.L., and E.L.F. Holzbaur. 2018. Motor Proteins. *Cold Spring Harb. Perspect. Biol.* 10:a021931. https://doi.org/10.1101/cshperspect.a021931

Tanenbaum, M.E., R.D. Vale, and R.J. McKenney. 2013. Cytoplasmic dynein crosslinks and slides anti-parallel microtubules using its two motor domains. *eLife.* 2:e00943. https://doi.org/10.7554/eLife.00943

Taveneau, C., R. Blanc, G. Péhau-Arnaudet, A. Di Cicco, and A. Bertin. 2020. Synergistic role of nucleotides and lipids for the self-assembly of Shs1 septin oligomers. *Biochem. J.* 477:2697–2714. https://doi.org/10.1042/BCJ20200199

Torraca, V., and S. Mostowy. 2016. Septins and Bacterial Infection. *Front. Cell Dev. Biol.* 4:127. https://doi.org/10.3389/fcell.2016.00127

Tortosa, E., Y. Adolfs, M. Fukata, R.J. Pasterkamp, L.C. Kapitein, and C.C. Hoogenraad. 2017. Dynamic Palmitoylation Targets MAP6 to the Axon to Promote Microtubule Stabilization during Neuronal Polarization. *Neuron.* 94:809–825.e7. https://doi.org/10.1016/j.neuron.2017.04.042

Traikov, S., C. Stange, T. Wassmer, P. Paul-Gilloteaux, J. Salamero, G. Raposo, and B. Hoflack. 2014. Septin6 and Septin7 GTP binding proteins regulate AP-3- and ESCRT-dependent multivesicular body biogenesis. *PLoS One.* 9:e109372. https://doi.org/10.1371/journal.pone.0109372

Urnavicius, L., C.K. Lau, M.M. Elshenawy, E. Morales-Rios, C. Motz, A. Yildiz, and A.P. Carter. 2018. Cryo-EM shows how dynactin recruits two dyneins for faster movement. *Nature.* 554:202–206. https://doi.org/10.1038/nature25462

Vaughan, K.T., and R.B. Vallee. 1995. Cytoplasmic dynein binds dynactin through a direct interaction between the intermediate chains and p150Glued. *J. Cell Biol.* 131:1507–1516. https://doi.org/10.1083/jcb.131.6.1507

Verdier-Pinard, P., D. Salaun, H. Bouguenina, S. Shimada, M. Pophillat, S. Audebert, E. Agavnian, S. Coslet, E. Charafe-Jauffret, T. Tachibana, and A. Badache. 2017. Septin 9_i2 is downregulated in tumors, impairs cancer cell migration and alters subnuclear actin filaments. *Sci. Rep.* 7:44976. https://doi.org/10.1038/srep44976

Weems, A., and M. McMurray. 2017. The step-wise pathway of septin heterooctamer assembly in budding yeast. *eLife.* 6:e23689. https://doi.org/10.7554/eLife.23689

Willett, R., J.A. Martina, J.P. Zewe, R. Wills, G.R.V. Hammond, and R. Puertollano. 2017. TFEB regulates lysosomal positioning by modulating TMEM55B expression and JIP4 recruitment to lysosomes. *Nat. Commun.* 8:1580. https://doi.org/10.1038/s41467-017-01871-z

Wilson, B.J., J.L. Allen, and P.T. Caswell. 2018. Vesicle trafficking pathways that direct cell migration in 3D matrices and in vivo. *Traffic.* 19:899–909. https://doi.org/10.1111/tra.12605

Yim, W.W., and N. Mizushima. 2020. Lysosome biology in autophagy. *Cell Discov.* 6:6. https://doi.org/10.1038/s41421-020-0141-7

Zent, E., and A. Wittinghofer. 2014. Human septin isoforms and the GDP-GTP cycle. *Biol. Chem.* 395:169–180. https://doi.org/10.1515/hsz-2013-0268

Zent, E., I. Vetter, and A. Wittinghofer. 2011. Structural and biochemical properties of Sept7, a unique septin required for filament formation. *Biol. Chem.* 392:791–797. https://doi.org/10.1515/BC.2011.082

Zhang, K., H.E. Foster, A. Rondelet, S.E. Lacey, N. Bahi-Buisson, A.W. Bird, and A.P. Carter. 2017. Cryo-EM Reveals How Human Cytoplasmic Dynein Is Auto-inhibited and Activated. *Cell.* 169:1303–1314.e18. https://doi.org/10.1016/j.cell.2017.05.025

Supplemental material

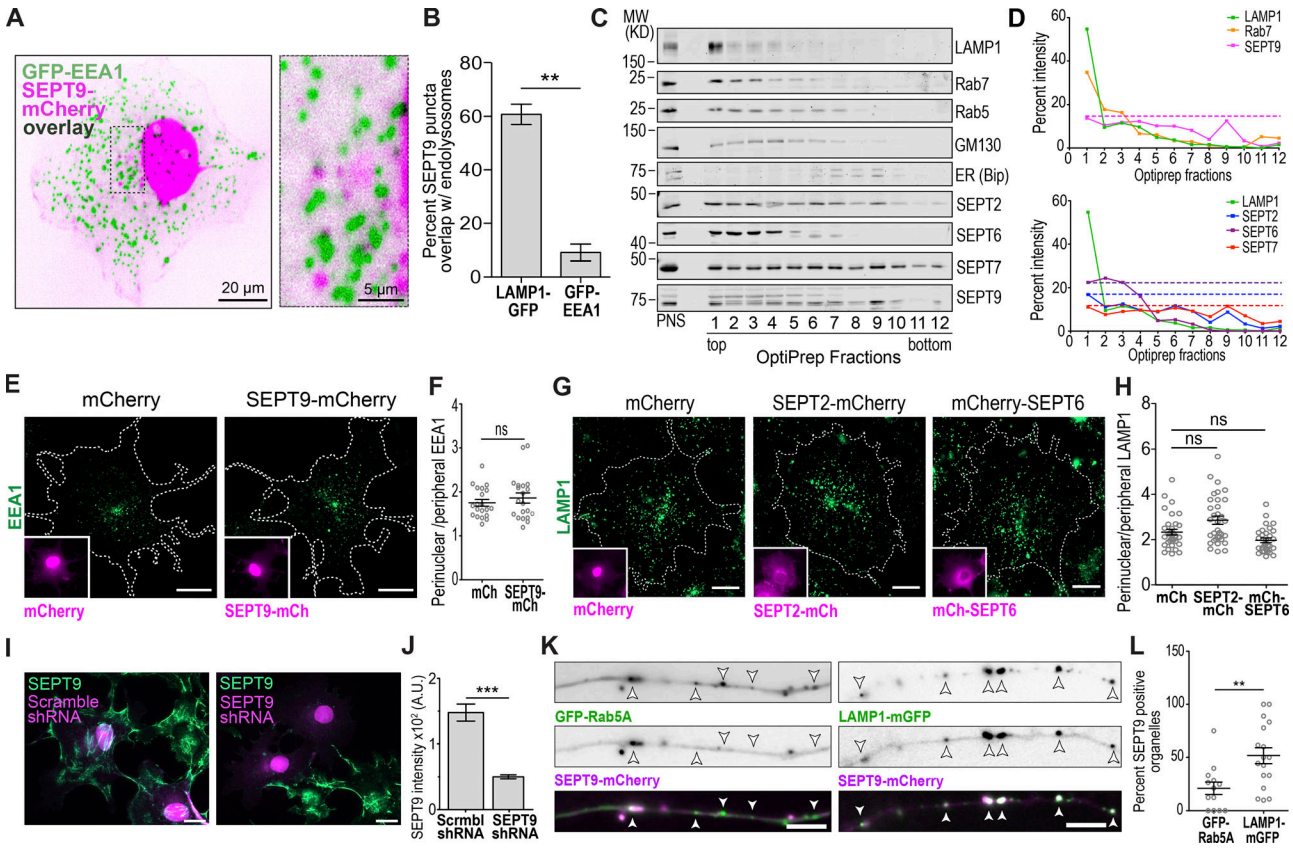

Figure S1. **Septin localization and effects on early endosomes and lysosomes. (A)** Spinning-disk confocal image shows the distribution of SEPT9-mCherry, which was expressed under the PGK promoter, with respect to GFP-EEA1 in living COS-7 cells. Scale bar, 20 µm. Perinuclear area is shown in higher magnification. Scale bar, 5 µm. **(B)** Quantification shows the fraction (mean ± SEM; Mann–Whitney *U* test) of SEPT9-mCherry puncta colocalizing with LAMP1-mGFP and GFP-EEA1 in COS-7 cells (n = 6). **(C and D)** PNSs of HEK-293 cell extracts were loaded on an iodixanol OPTIPREP density gradient (17%, 20%, 23%, 27%, and 30%), and fractions were blotted (C) for LAMP-1, Rab7, Rab5, GM130, BIP, SEPT9, SEPT2, SEPT6, and SEPT7. Plots (D) show quantification of indicated proteins in each fraction as percentage of total proteins across all fractions. Horizontal dashed lines provide a reference point for the percentage of septin protein in the top fraction. **(E and F)** Images (E) show the distribution of early endosomes (EEA1) in COS-7 cells that overexpress mCherry or SEPT9-mCherry (insets). Scale bars, 20 µm. Quantification (F) shows the ratio (mean ± SEM; unpaired *t* test) of perinuclear to peripheral fluorescence intensity of EEA1 per cell (n = 20). **(G and H)** Images (G) of LAMP1-stained COS-7 cells expressing mCherry, SEPT2-mCherry, or mCherry-SEPT6 (insets). Scale bars, 20 µm. Plot (H) shows the ratio (mean ± SEM; Kruskal–Wallis one-way ANOVA) of perinuclear to peripheral fluorescence intensity of LAMP1 per cell (n = 30–34). **(I and J)** Images (I) of COS-7 cells, which were transfected with plasmids that coexpress GFP and scramble or SEPT9 shRNA and stained with anti-SEPT9 antibody. Scale bars, 20 µm. Bar graph (J) shows fluorescence intensity (mean ± SEM; Mann–Whitney *U* test) of SEPT9 per shRNA-expressing cell (n = 27–35). A.U., arbitrary units. **(K and L)** Images (K) of axon segments in hippocampal neurons (DIV4), which were cotransfected with rat SEPT9-mCherry and GFP-Rab5A or LAMP1-mGFP. Scale bars, 5 µm. Plot (L) shows percentage (mean ± SEM; Mann–Whitney *U* test) of GFP-Rab5A (n = 13 axons) and LAMP1-mGFP (n = 17 axons) puncta with SEPT9-mCherry per cell. ns, nonsignificant ($P > 0.05$); **, $P < 0.01$; ***, $P < 0.001$.

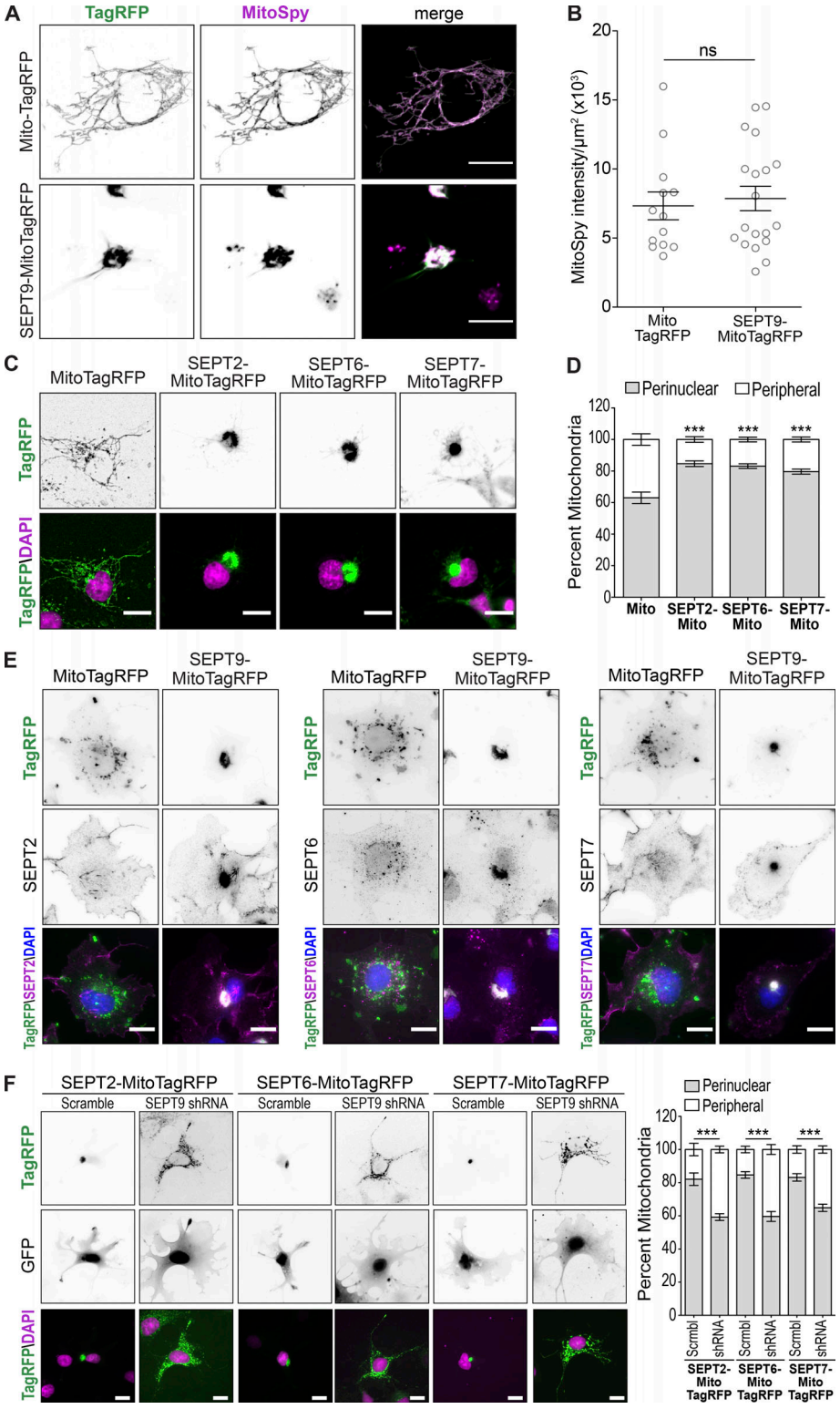

Figure S2. **Targeting of septins to mitochondria induces perinuclear clustering in a SEPT9-dependent manner. (A and B)** Images (A) show localization of MitoTagRFP- and SEPT9-MitoTagRFP-labeled mitochondria in living COS-7 cells, which were labeled with MitoSpy as an indicator of cell and mitochondria health. Plot (B) shows the fluorescence intensity (mean ± SEM; Mann–Whitney *U* test) of MitoSpy per mitochondria (MitoTagRFP) surface area per cell (n = 13–19). Scale bars, 20 µm. **(C and D)** Images (C) show DAPI-stained COS-7 cells, which were transfected with MitoTagRFP (control) or MitoTagRFP-tagged SEPT2, SEPT6, and SEPT7. Scale bars, 20 µm. Bar graph (D) shows percentage (mean ± SEM; two-way ANOVA; n = 20–28 cells) of total mitochondria fluorescence intensity in the perinuclear and peripheral cytoplasm. **(E)** Images show COS-7 cells transfected with MitoTagRFP or SEPT9-MitoTagRFP and stained with antibodies against SEPT2, SEPT6, and SEPT7. Scale bars, 20 µm. **(F)** Images of DAPI-stained COS-7 cells after cotransfection with scramble or SEPT9 shRNAs (GFP) with MitoTagRFP-tagged SEPT2, SEPT6, or SEPT7. Scale bars, 20 µm. Bar graph shows the percentage of perinuclear and peripheral mitochondria (mean ± SEM; two-way ANOVA; n = 24–35 cells) in the indicated conditions. ns, nonsignificant ($P > 0.05$); ***, $P < 0.001$.

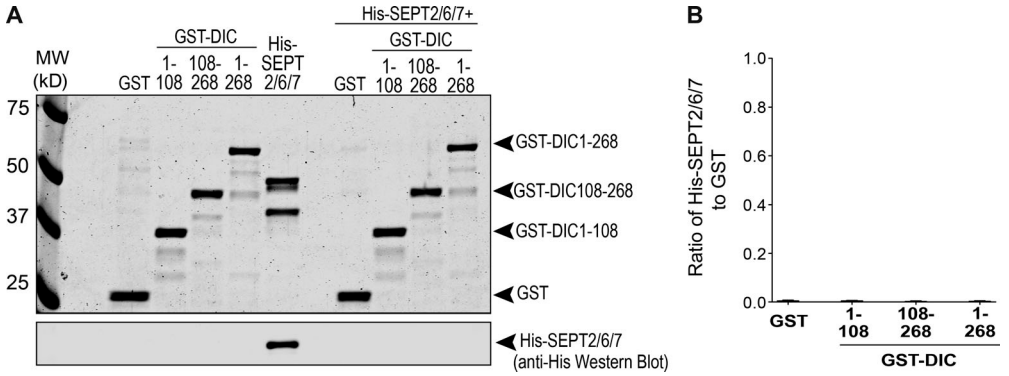

Figure S3. **SEPT2/6/7 does not interact with DIC. (A)** Coomassie-stained gel (top) and Western blot (bottom; anti-His) show results from pull-down assays of purified recombinant His-SEPT2/6/7 with GST (control) or GST-tagged DIC(1–108), DIC(108–268), and DIC(1–268). **(B)** Bar graph shows ratio (mean ± SEM) of His-SEPT2/6/7 to GST and GST-DIC fragments from three independent experiments.

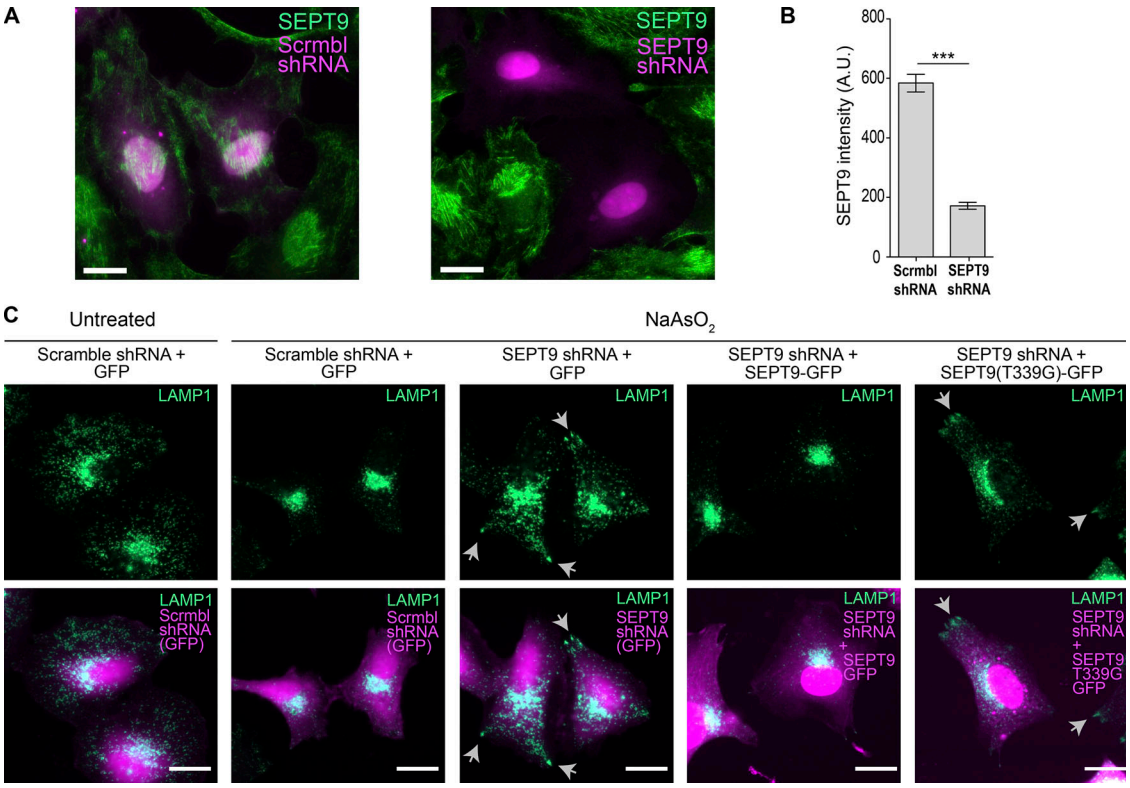

Figure S4. **SEPT9 promotes perinuclear clustering of lysosomes in HeLa cells under oxidative stress. (A)** Images show SEPT9-stained HeLa cells after transfection with plasmids that coexpress GFP (magenta) and scramble or SEPT9 shRNAs. Scale bars, 20 µm. **(B)** Bar graph shows mean (± SEM; Mann–Whitney *U* test) fluorescence intensity of SEPT9 per shRNA-expressing cell (n = 65–66). ***, P < 0.001. A.U., arbitrary units. **(C)** HeLa cells were transfected with plasmids that coexpress shRNAs (scramble control or SEPT9) and GFP or shRNA-resistant SEPT9-GFP (wild type or T339G mutant; magenta). After treatment with $NaAsO_2$ (400 µM) for 1 h, cells were stained with antibodies against LAMP1 (green). Representative images show LAMP1 (green) and GFP or SEPT9-GFP (magenta). Arrows point to lysosomes that localize to the periphery of SEPT9-depleted and SEPT9(T339G)-GFP–expressing cells. Quantifications of lysosome localization are shown in Fig. 5, F and G. Scale bars, 20 µm.

Video 1. **COS-7 cells were cotransfected with LAMP1-mGFP and SEPT9_i1-mCherry under the control of a weak PGK promoter and imaged every 3 s by spinning-disk microscopy.** Arrowheads point to SEPT9-positive lysosomes moving retrogradely. SEPT9_i1-mCherry is pseudo-colored in inverted magenta, and LAMP1-mGFP is pseudo-colored in inverted green. Scale bar, 20 µm. Video display rate is 5 frames per second. Related to Fig. 1.

Video 2. **Rat embryonic hippocampal neurons (DIV4) were cotransfected with mCherry and LAMP1-mGFP and imaged with shallow-angle TIRF microscopy every 1 s for 2 min.** mCherry is pseudo-colored in magenta, and Lamp1-mGFP is pseudo-colored in green. Video display rate is 15 frames per second. Neuronal cell body (soma) is located to the left of the axonal segment of the video (i.e., particles move retrogradely to the left and anterogradely to the right). Scale bar, 5 µm. Related to Fig. 1.

Video 3. **Rat embryonic hippocampal neurons (DIV4) were cotransfected with rat SEPT9_i1-mCherry and LAMP1-mGFP and imaged with shallow-angle TIRF microscopy every 1 s for 2 min.** Rat SEPT9_i1-mCherry is pseudo-colored in magenta, and LAMP1-mGFP is pseudo-colored in green. Video display rate is 15 frames per second. Neuronal cell body (soma) is located to the left to the axonal segment of the video (i.e., particles move retrogradely to the left and anterogradely to the right). Scale bar, 5 µm. Related to Fig. 1.